small methods
www.small-methods.com

# In Situ and Operando Analytical Techniques of Single-Atom Catalysts for Electrocatalytic $CO_2$ Reduction

*Rongbo Sun, Xingyun Liu, Jingyao Huang, Yuchao Wang, Hongwen Huang, Yongpeng Lei,* and Jingjie Ge**

**Electrocatalytic technology, which facilitates the transformation of carbon dioxide ($CO_2$) into high-value chemicals, stands as one of the most hopeful approaches for $CO_2$ utilization. Single-atom catalysts (SACs) are promising for catalyzing $CO_2$ reduction reactions ($CO_2$RR) owing to the tunable electronic structures of their central metal atoms, which enable precise control over the adsorption energies of reactants and intermediates. Additionally, SACs bridge the gap between homogeneous and heterogeneous catalysts, offering an ideal platform to investigate the reaction mechanisms of $CO_2$RR. Therefore, gaining a comprehensive understanding of the intrinsic structural evolution of SACs, along with the micro-environmental changes around active sites and electrode interfaces under operational conditions, is crucial for designing effective electrocatalysts and devices for $CO_2$RR. This review introduces the fundamentals underlying the electrocatalytic $CO_2$RR. Subsequently, the key techniques for SACs identification and validation are thoroughly analyzed, laying a theoretical basis for the case studies. Third, the latest development of in situ and operando analytical techniques of SACs toward $CO_2$RR are summarized, including infrared spectroscopy (IR), Raman spectroscopy, X-ray absorption spectroscopy (XAS), and transmission electron microscopy (TEM). Finally, several issues are raised and possible solutions are offered regarding the in situ and operando analytical techniques of SACs for the $CO_2$RR.**

## 1. Introduction

The extensive dependence on fossil fuel sources, such as oil, coal, and natural gas, has significantly increased carbon dioxide ($CO_2$) emissions, exacerbating the global warming crisis[1] Electrocatalytic technology, which reduces $CO_2$ to fuels and chemicals, is currently one of the most attractive ways of $CO_2$ utilization, facilitating the establishment of a carbon-neutral cycle.[2] Significant and continuous advancements have been made in the electrocatalytic $CO_2$ reduction reaction ($CO_2$RR) over the last decade, $CO_2$ is reduced to various products by different reaction pathways.[3,4] However, elucidating the reaction mechanism remains challenging due to the intrinsic complexity of the process, which arises from proton-coupled electron transfer and the involvement of numerous highly reactive intermediates.[5,6] There are inherent limitations associated with using traditional ex situ characterization techniques

R. Sun, J. Huang
Sinochem Holdings Corporation Ltd.
Sinochem Energy High-tech Corporation Ltd.
2 West Tieying Middle Rd., Fengtai District, Beijing 100031, China
X. Liu
Division of Life Sciences and Medicine
Department of Oncology
The First Affiliated Hospital of USTC
Center for Advanced Interdisciplinary Science and Biomedicine of IHM
University of Science and Technology of China
Hefei, Anhui 230601, China

H. Huang
Key Laboratory of Mesoscopic Chemistry of MOE
Jiangsu Provincial Laboratory for Nanotechnology
School of Chemistry and Chemical Engineering
Nanjing University
Nanjing 210023, China
Y. Wang, Y. Lei
State Key Laboratory of Powder Metallurgy
Central South University
Changsha 410083, China
E-mail: leiyongpeng@csu.edu.cn
J. Ge
Department of Applied Biology and Chemical Technology
The Hong Kong Polytechnic University
Hung Hom, Kowloon, Hong Kong 999077, China
E-mail: jingjie.ge@polyu.edu.hk

The ORCID identification number(s) for the author(s) of this article can be found under https://doi.org/10.1002/smtd.202500516



**DOI: 10.1002/smtd.202500516**

for investigating the reaction mechanisms in the reaction process.[7] For example, these techniques are incapable of monitoring transient reaction intermediates or capturing the dynamic transitions that occur during the real electrocatalytic process.[8] Furthermore, ex situ analysis risks altering catalyst morphology or oxidation states during sample transfer or pre-treatment, potentially resulting in inaccurate conclusions regarding active sites or intermediate species.

To address the discrepancy between the underperformances of electrocatalysts and the demanding technical prerequisites for future applications, it is imperative to explore an effective solution to gain a deep comprehension of active sites, intermediates, and reaction mechanisms involved in the $CO_2$RR process.[9,10] Currently, a range of in situ characterization techniques have been employed to elucidate the process of structural transformation. Particularly, researchers have paid increasing attention to leveraging synchrotron radiation techniques to investigate reaction mechanisms under diverse operation conditions.[11,12] As an emerging research frontier, single-atom catalysts (SACs) exhibit significant potential in the field of $CO_2$RR owing to their distinctive geometric and electronic configurations.[13,14] Furthermore, SACs with precisely engineered structures have emerged as an exemplary model for discerning reaction mechanisms and comprehending the relationship between the structure and function of electrocatalysts in the $CO_2$RR.[15] Consequently, the recent advancements in the application of in situ and operando analytical techniques in SACs for $CO_2$RR systems merit comprehensive investigation.

Techniques such as infrared (IR) spectroscopy, X-ray absorption spectroscopy (XAS), transmission electron microscopy (TEM), and Raman spectroscopy are particularly noteworthy in this context. For example, in situ IR spectroscopy enables real-time tracking of reaction products and surface-adsorbed intermediates, offering direct insights into reaction pathways and active site functionality.[16,17] XAS provides atomic-resolution information on the electronic states and local coordination environments of metal centers.[18] And in situ TEM bridges macro-to-atomic scales by directly visualizing morphological changes and lattice distortions of SACs.[19] Raman spectroscopy complements these approaches by identifying vibrational signatures of non-polar species and surface reconstruction phenomena under bias.[20,21] Collectively, these technologies can form a synergistic toolkit, which is crucial for advancing the understanding of $CO_2$RR mechanisms and rational catalyst design.

Herein, we provide an overview of SACs for the electrocatalytic $CO_2$RR to valuable products with in situ characterization and mechanism studies, thereby facilitating the development of highly efficient $CO_2$RR electrocatalysts. Initially, we systematically outline the fundamental mechanisms underlying the formation of $CO_2$RR products from the theoretical perspective. Subsequently, we thoroughly analyze the key techniques for SACs identification and validation. Then, we summarize and analyze the development and applications of advanced characterization techniques of SACs in $CO_2$RR systems. Finally, based on the latest advancements, we elucidate the prospective opportunities and delineate the outstanding challenges that remain for future investigations of SACs for the electrocatalytic reduction of $CO_2$ (**Figure 1**).

## 2. Mechanism of the Electrocatalytic $CO_2$ Reduction

The $CO_2$RR is a multifaceted process characterized by multiple proton-coupled electron transfer (PCET) steps, which correspond to various reaction pathways involving 2 to 18 electron transfers.[22] This complexity leads to a diverse array of products, including $C_1$ products (such as CO, HCOOH, $CH_3OH$, HCHO, and $CH_4$) and $C_{2+}$ products (such as $C_2H_4$, $C_2H_5OH$, $CH_3COOH$, and $CH_3COCH_3$).[23,24] Typically, the catalytic reactions on most SACs involve two-electron transfer processes in $CO_2$RR, predominantly yielding CO or HCOOH as the reduction products.[25] The primary advantages of SACs in $CO_2$RR encompass their precisely defined active sites, high atomic utilization efficiency, reduced overpotentials, and effective suppression of the HER. Notably, the intrinsic activity of SACs can be engineered by modifying the central active site, enabling the selective production of CO, formate, and/or other value-added chemicals from $CO_2$RR. By strategically engineering the coordination environment, including altering the coordination number, modifying the coordinating atoms, or introducing heteroatom dopants, could disrupt the symmetric structure of the original M-$N_4$ sites, ultimately influencing the catalyst's activity and selectivity for a given product.[26]

To enhance the understanding of SAC for $CO_2$RR, it is imperative to integrate advanced in situ and operando characterization techniques, including coupled multi-modal in situ characterization methods, alongside theoretical calculations. In this section, we summarize the potential reaction pathways for $C_1$ products and the principal $C_{2+}$ products, grounded in the contemporary dominant comprehension of $CO_2$RR mechanisms, to facilitate the rational design of SACs that exhibit high activity, selectivity, and stability.

### 2.1. Mechanism of Product Formation

#### *2.1.1. Pathways for $C_1$ Products*

Despite considerable research efforts aimed at elucidating the pathways for CO generation, the reaction mechanism continues to be debated. Currently, the conversion of $CO_2$ into CO via $^*$COOH intermediates is well-established in the literature. This transformation can occur via a PCET process or a proton transfer following an initial electron transfer (**Figure 2**).[27,28] The $^*$COOH intermediate is expected to undergo a subsequent PCET process, forming $^*$CO. It is expected that the weakly bound $^*$CO desorbs from the surface of the catalyst, leading to the production of CO. In synthesizing various $C_1$ products (such as HCHO, $CH_3OH$, and $CH_4$), $^*$CO is widely recognized as a significant intermediate.[29] Peterson's group has shown that the most favorable stable route for the $CO_2$RR on the Cu (211) surface involves the generation of $^*$CO, which is subsequently hydrogenated to yield $^*$HCO, $^*H_2CO$, and $^*H_3CO$.[30] Among the various species, $^*H_2CO$ can selectively desorb, forming either HCHO or $^*H_3CO$. The $^*H_3CO$ species can subsequently undergo a PCET process to yield $CH_3OH$. Nie's group proposed a plausible mechanism for the synthesis of $CH_4$ based on theoretical analysis. In this proposed pathway, $^*$CO is posited to produce the $^*$COH intermediate, which subsequently undergoes reduction to yield adsorbed

 

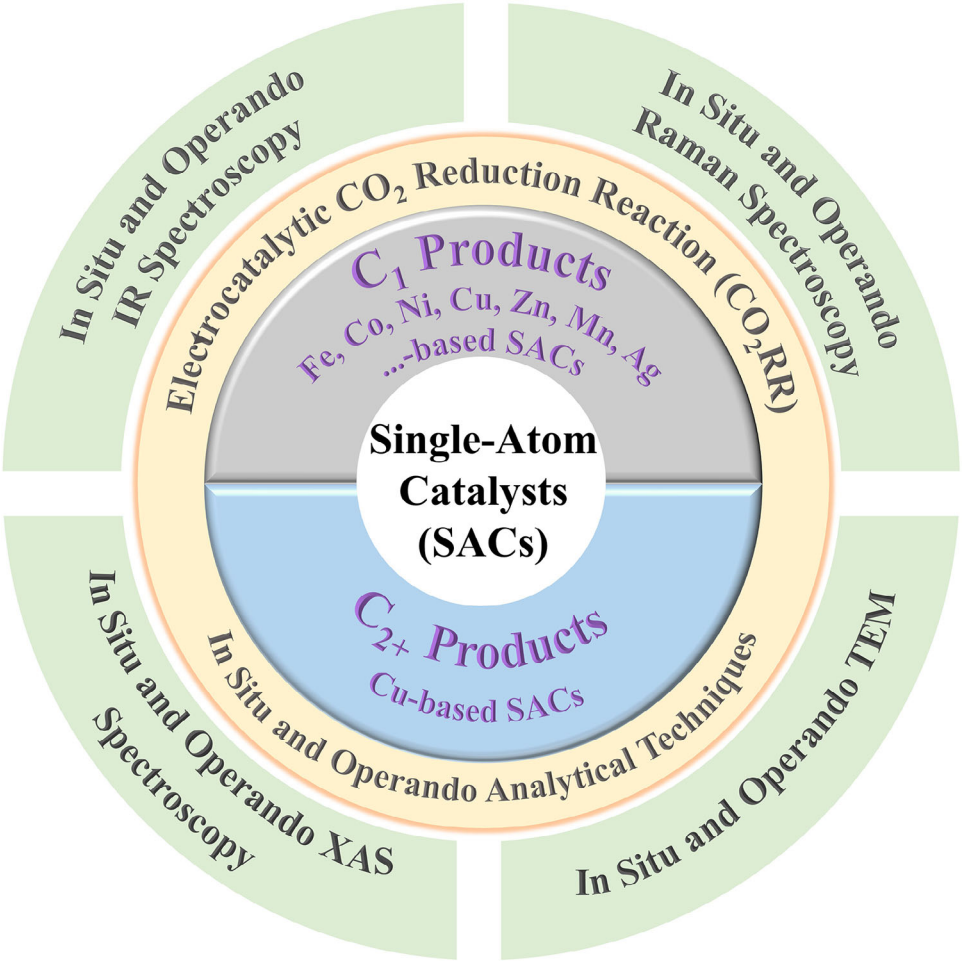


**Figure 1.** Schematic overview of the in situ and operando analytical techniques in SACs for $CO_2RR$.

$^*C$. This intermediate is subsequently reduced sequentially to produce $^*CH$, $^*CH_2$, $^*CH_3$, ultimately forming the final product, $CH_4$.[23]

CO is the predominant $C_1$ product of the $CO_2RR$, and a substantial number of SACs, including Fe, Co, Ni, and Mn, demonstrate a high selectivity for CO production, markedly distinct from their bulk metal counterparts in terms of catalytic performance.[29] Liu et al. developed a universal two-step strategy for the construction of structurally well-defined Ni-SAC models to investigate $CO_2RR$. Operando spectroscopic analyses combined with electrochemical kinetics studies identified the rate-determining step (RDS) as the PCET process: $^*CO_2^- + H^+ \rightarrow {}^*COOH$. Subsequently, the adsorbed CO intermediates desorbed from the active sites, releasing CO as the final gaseous product.[31] Cao et al. designed a series of transition metal-based single-atom catalysts (TM–$N_2O_2C_x$, where TM = Sc, Ti, V, Cr, Mn, Fe, Co, Ni, Cu, and Zn) and systematically investigated their electrocatalytic mechanism for $CO_2RR$ via density functional theory (DFT) calculations. These TM–$N_2O_2C_x$ catalysts demonstrated excellent product selectivity toward CO, $CH_4$, and HCOOH. Specifically, Sc–$N_2O_2C_x$, Mn–$N_2O_2C_y$, and Zn–$N_2O_2C_x$ favored CO formation, while V–$N_2O_2C_x$ selectively produced $CH_4$. The remaining six catalysts predominantly yielded HCOOH. Furthermore, the most favorable reaction pathway for $CH_4$ generation was elucidated as follows: $^* + CO_2 \rightarrow {}^*COOH \rightarrow {}^*CO + H_2O \rightarrow {}^*CHO \rightarrow {}^*CH_2O \rightarrow {}^*CH + H_2O \rightarrow CH_2 \rightarrow CH_3 \rightarrow {}^* + CH_4$.[32]

In contrast to other $C_1$ products, the formation of HCOOH or $HCOO^-$ follows a distinct reaction pathway. The synthesis of HCOOH or $HCOO^-$ can occur via an intermediate, which is primarily facilitated by the adsorption of oxygen atoms onto the catalyst surface. Currently, In, Sn, Sb, Cu, and Mo-based SACs have demonstrated significant selectivity toward formate ($HCOO^-$) production.[33] Since most $CO_2RR$ are carried out in alkaline or neutral electrolytes, the product is usually formate rather than formic acid. However, recent studies have explored conducting $CO_2RR$ in a highly acidic medium to directly obtain formic acid, which is anticipated to reduce overall product regeneration costs.[34]

### 2.1.2. Pathways for $C_{2+}$ Products

The reaction mechanisms associated with $C_{2+}$ products exhibit a notable degree of complexity. This section overviews the potential reaction pathways for the two main $C_{2+}$ products: $C_2H_4$ and $C_2H_5OH$ (Figure 2).[35,36] $^*CO$ is identified as a critical

 

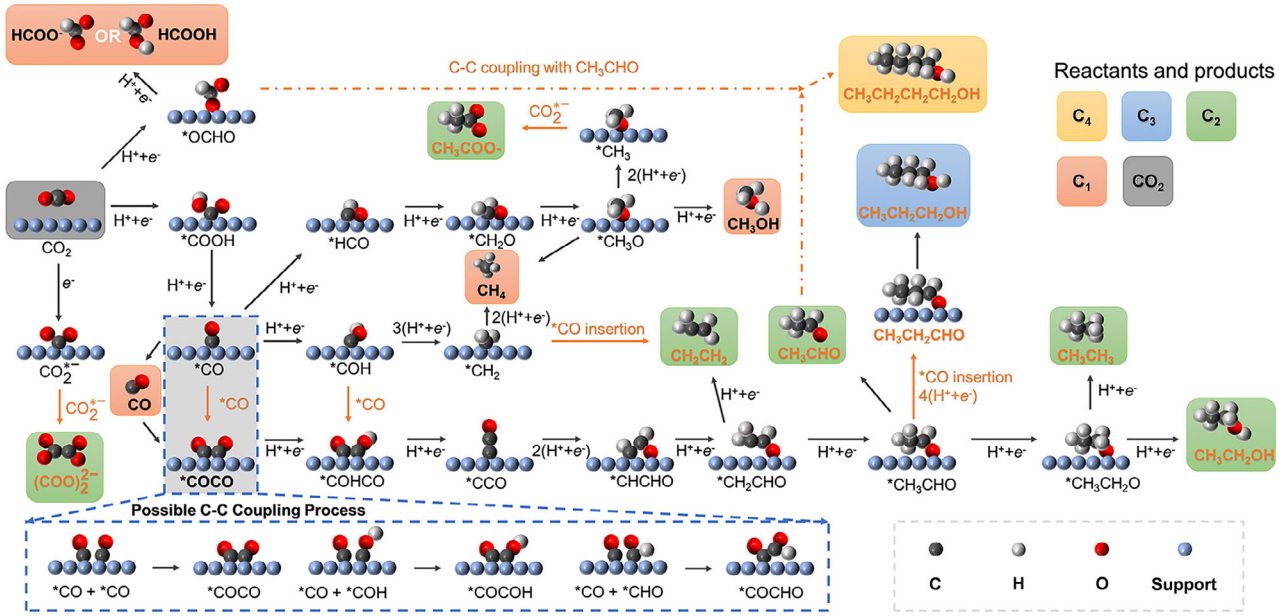


**Figure 2.** Possible reaction route to $C_1$–$C_4$ carbon-containing products from $CO_2$ electroreduction. Some typical $C_1$, $C_2$, $C_3$, and $C_4$ products are highlighted in red, green, blue, and yellow frames, respectively. The blue dashed rectangle demonstrates three possible C–C coupling process routes. Reproduced with permission. Ref. [36] Copyright 2023, American Chemical Society.

intermediate in the synthesis of $C_{2+}$ products. This intermediate can be directly converted into the $^*C_2HO_2$ intermediate via a process of symmetric dimerization, which is subsequently followed by hydrogenation. Alternatively, $^*CO$ may be hydrogenated first, and the resulting $^*CHO$ or $^*COH$ intermediate is asymmetric with $^*CO$ to produce the $^*C_2HO_2$ intermediate.[37] Several PCET steps occur following the C–C coupling process, forming the critical $^*C_2H_3O$ intermediate, which is instrumental in synthesizing $C_2H_4$ and $C_2H_5OH$. Notably, in most catalytic systems, the selectivity for $C_2H_4$ surpasses that for $C_2H_5OH$, as the energy barrier from the $^*C_2H_3O$ intermediate to the $C_2H_4$ product is lower than for the $C_2H_5OH$ product.[38]

Obtaining multi-carbon products using SACs presents a significant challenge to couple multiple reaction intermediates at isolated active sites.[39] In the catalysts that have been synthesized to date, Cu-based catalysts are uniquely recognized for their ability to facilitate the electrochemical reduction of $CO_2RR$ to $C_{2+}$ products, attributed to their moderate binding energy with $^*CO$.[40] C–C coupling on Cu-SACs can be achieved through strategies such as 1) building diatomic (two-atom) sites; 2) facilitating the reversible transformation between isolated Cu atoms and Cu nanoparticles; 3) exploiting synergistic interactions between the Cu center and its coordinating atoms.[41]

## 3. Key Techniques for Single-Atom Catalysts Identification and Validation

Elucidating the geometric and electronic of SACs is important to understanding their structure-performance correlations in $CO_2RR$. Conventional characterization techniques such as X-ray diffraction (XRD), X-ray photoelectron spectroscopy (XPS), and Raman spectroscopy provide limited atomic-level structural analysis of SACs. Advanced analytical methods, specifically aberration-corrected high-angle annular dark-field scanning transmission electron microscopy (AC-HAADF-STEM) and XAS are essential for accurately determining SACs' structural and electronic properties.[42]

### 3.1. AC-HAADF-STEM

Driven by the rapid advancement of SACs in recent years, AC-HAADF-STEM has emerged as a critical tool for the identification and analysis of atomically dispersed active sites. Metal atoms supported on solid carriers are commonly characterized using AC-HAADF-STEM. Atoms with higher atomic numbers (Z) scatter electrons more strongly and at higher angles due to the increased electrostatic interaction between the metal atomic nucleus and the incident electron beam. If the metal atom has a higher atomic number than the support, anchored metal atoms appear as bright spots in aberration-corrected STEM images.[43] As a pioneering example, Chung et al. reported single Fe atoms supported on carbon. Through the combined use of AC-HAADF-STEM and EELS, the direct observation of the $Fe–N_4$ configuration was achieved.[44] AC-HAADF-STEM enables the visualization of individual metal atoms supported on solid carriers, particularly carbon supports, by exploiting differences in Z-contrast. However, AC-HAADF-STEM is still limited in probing the electronic state and coordination configuration of metal active sites currently.

### 3.2. XAS

XAS, encompassing X-ray absorption near-edge structure (XANES) and extended X-ray absorption fine structure (EXAFS),

 

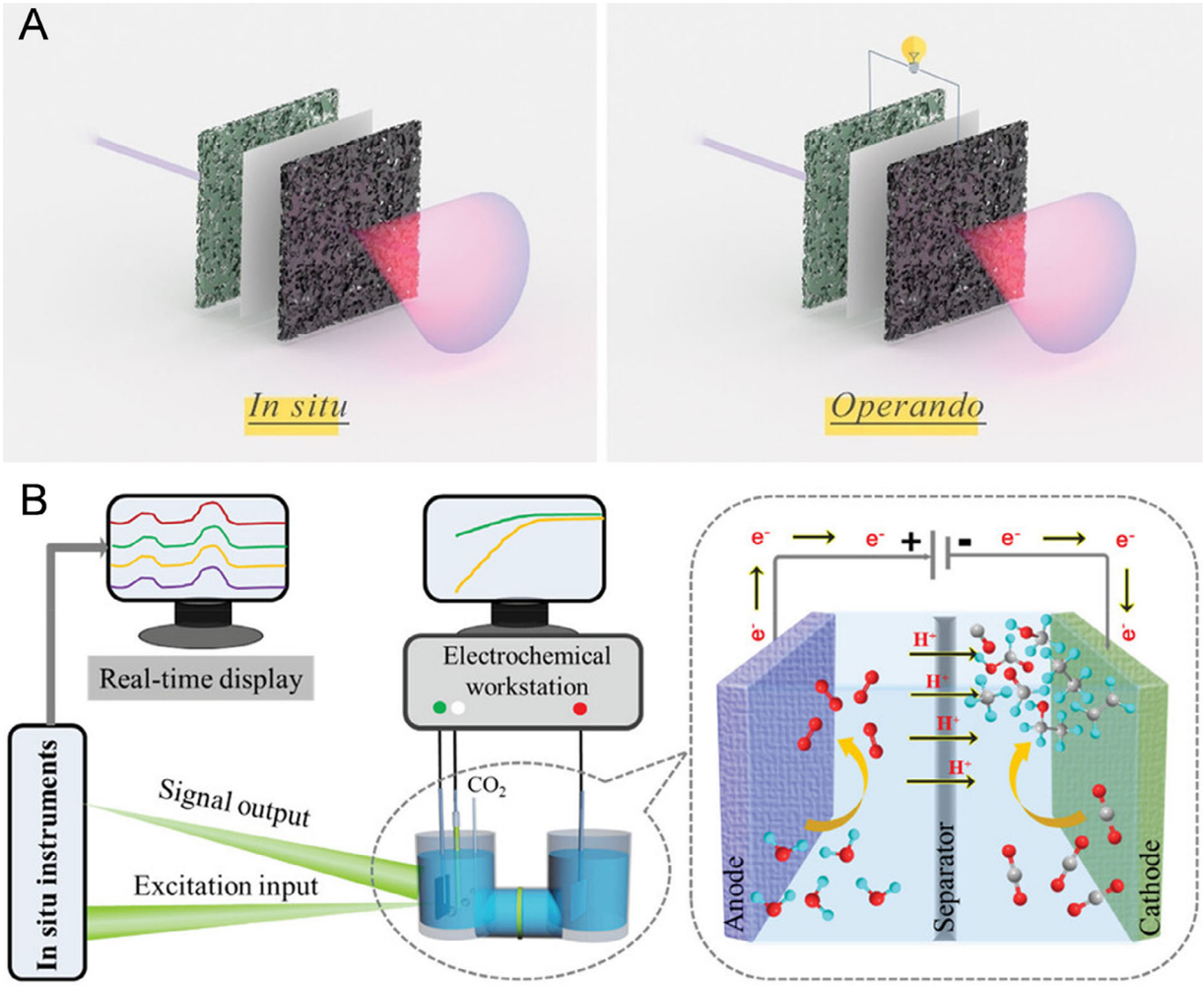


**Figure 3.** A) Schematic diagram of in situ versus operando experiments. Operando requires that the cycling be continuously performed and not stopped during the structural characterization with permission. Ref. [56] Copyright 2021, Wiley-VCH. B) Schematic diagram of the basic configuration of in situ instruments. The right half is the schematic representation of electrochemical cells for $CO_2$RR. Elements C, H, and O are represented by gray, blue, and red balls, respectively. Reproduced with permission. Ref. [12] Copyright 2021, Wiley-VCH.

offers a robust approach for characterizing the electronic state, coordination, and geometric structure of single-atom sites.[43] XANES is highly sensitive in capturing information related to average valence states and electron configurations. The near-edge position in XANES spectra corresponds to the oxidation state of the target element, with higher oxidation states requiring greater energy for core electron excitation. EXAFS provides key details regarding the local geometry and coordination environment of single-atom sites. Fitting the EXAFS data allows for the quantitative determination of parameters like bond lengths and coordination numbers. In addition, analysis of the EXAFS data provides valuable insights into the bonding and coordination configuration of the metal center.[45]

Furthermore, additional characterization techniques including IR, electron paramagnetic resonance (EPR), nuclear magnetic resonance (NMR), low-energy ion scattering (LEIS), and Mössbauer spectroscopy can offer valuable structural and electronic information about SACs.[46,47]

## 4. Real-Time Analysis of Single-Atom Catalysts for $CO_2$ Electroreduction

Over the past decade, the field of $CO_2$ electroreduction has witnessed significant and continuous advancements.[48–50] Nonetheless, understanding the reaction mechanism continues to be a formidable challenge due to the complexity of the process, driven by the transfer of multiple protons and electrons, as well as the presence of various highly reactive intermediates.[51] Investigating the interactions among catalyst structure, product selectivity, reaction conditions (e.g., temperature and time), and reaction intermediates in electrochemical processes is essential for advancing the design of more effective catalysts, interfaces, and reactors. Ex situ methodologies, such as diffraction, microscopy, and spectroscopy, can yield significant information regarding the structural, compositional, physical, and chemical characteristics of the electrode. Nevertheless, given the dynamic characteristics of the three-phase interface (comprising the electrolyte, catalyst, and

 

**Table 1.** The advantages and limitations of in situ and operando characterization techniques.

| Techniques | Advantages | Limitations |
|---|---|---|
| IR | 1) Detecting reaction intermediates<br>2) Non-destructive | 1) Limited spatial resolution<br>2) Interference from gas/liquid phases<br>3) Overlapping absorption bands complicate the analysis |
| Raman | 1) Simple and highly accessible<br>2) Aqueous electrolytes can be used<br>3) Non-destructive | 1) Fluorescence interference<br>2) Weak signal intensity<br>3) Laser-induced heating may alter samples<br>4) Spatial resolution limited (~μm scale) |
| XAS | 1) Detecting element-specific local structure/oxidation states<br>2) Does not require crystalline samples | 1) Describing average information on local structures<br>2) Requires synchrotron radiation<br>3) Complex data analysis (needs reference spectra) |
| TEM | 1) Atomic-scale spatial resolution<br>2) Direct imaging<br>3) Captures dynamic processes in real-time | 1) Small imaging range<br>2) Operating conditions are relatively strict<br>3) Beam damage alters samples |

reactant), relying on ectopic techniques alone may be insufficient to elucidate mechanistic details under realistic conditions.[52,53] In situ and operando measurements can yield crucial insights into catalyst surfaces, electrode-electrolyte interfaces, products, and reaction intermediates.[54,55] The in situ technique represents real-time characterization conducted under controlled laboratory conditions that replicate operational environments. This approach facilitates a more precise understanding of the underlying mechanisms, albeit with limitations imposed by specific electrochemical environments. In contrast, operando refers to diagnostics carried out within fully operational devices under real-world service conditions, such as those involving high current densities, gas diffusion electrode configurations, and flowing electrolytes. Meanwhile, operando requires that the cycling be continuously performed and not stopped during the structural characterization (**Figure 3A**).[56–58] A schematic representation of the fundamental configuration of in situ instruments is illustrated in Figure 3B.[12]

In situ and operando techniques offer valuable insights into addressing the diverse challenges of the electrocatalytic $CO_2$RR. These challenges encompass 1) the surface morphology, reconstruction, chemical state, and stability; 2) the identification and quantification of active sites; 3) the characteristics of the electrode-electrolyte interface; and 4) the detection and monitoring of reaction intermediates and products.[59,60] The commonly employed in situ and operando techniques encompass IR, Raman, XAS, TEM, etc.[61–64] A comprehensive summary of their advantages and limitations is presented in **Table 1**. Furthermore, several novel in situ methodologies, such as on-chip in situ transport investigations and high-resolution neutron imaging, have recently been introduced.[65,66] SACs are characterized by individual metal atoms dispersed on a support material, with each active metal site serving as an idealized, simplified model for catalytic reactions. This uniform distribution imparts SACs excellent performance, enabling precise control over the coordination environment and electronic structure of each active site.[67,68] Importantly, the monatomic configuration of these catalysts facilitates the exploration of complex interactions between metal atoms, substrates, and reactive species. Through the application of advanced in situ and operando techniques, researchers are able to directly observe and monitor the dynamic behavior of individual metal atoms during catalysis, offering profound insights into fundamental reaction mechanisms at the atomic level.[69]

### 4.1. In Situ and Operando Infrared Spectroscopy

Attenuated total reflection (ATR) mode surface-enhanced infrared absorption spectroscopy (SEIRAS) is one of the most widely utilized techniques in spectroelectrochemistry.[70] The ATR-SEIRAS cell comprises two compartments separated by a Nafion membrane (**Figure 4A**). A thin metal catalyst layer is deposited on a Si (or Ge) crystal, functioning as the working electrode. The infrared beam undergoes internal reflection at the silicon-metal interface, generating evanescent waves that penetrate the adjacent solution (Figure 4B). The metal layer amplifies these evanescent waves, enabling the selective detection of species located within ≈1–10 nm of the electrode surface. This high surface sensitivity allows SEIRAS to in situ identify surface-bound species and reaction intermediates formed during the $CO_2$RR process. For example, Hao et al. employed the in situ ATR-SEIRAS technique to monitor reaction intermediates and clarify the reaction pathway of $CO_2$ reduction on Zn single-atom sites during the $CO_2$RR process.[71] As shown in Figure 4C, the absorption peaks at ≈1650 and ≈1380 $cm^{-1}$ were assigned to the H—O—H bending of interfacial water and the C—O stretching in $^*$COOH intermediate, respectively. The strong absorption peaks of $H_2O$ and $^*$COOH in the in situ ATR-SEIRAS spectra of $Zn_1NC$ suggested a favorable coupling between the adsorption and activation of $H_2O$ and $CO_2$ molecules on $ZnN_4$ single-atom sites, which promoted the $^*$H dissociation from $H_2O$ and the $^*$COOH formation via $^*CO_2$ protonation.

Zhao et al. loaded atomically dispersed Cu onto 1,3,5-triynylbenzene support and designed a SAC with a Cu—$C_2$ coordination structure.[72] This study used in situ monitoring

 

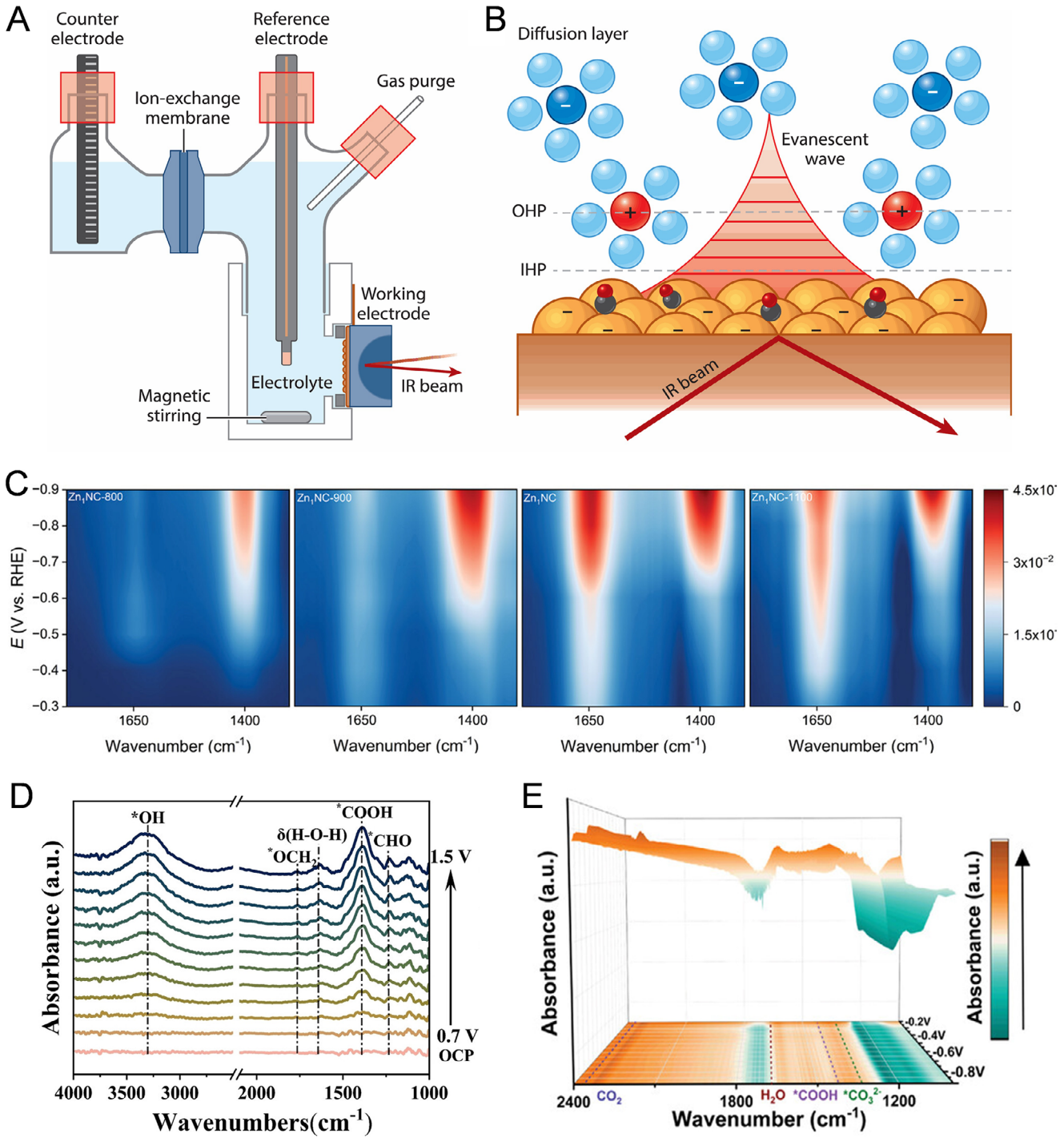


**Figure 4.** A) Schematic of electrochemical ATR-SEIRAS cell design. B) Schematic of the electrochemical double layer in SEIRAS experiments. Abbreviations: IHP, inner Helmholtz plane; OHP, outer Helmholtz plane. Reproduced with permission. Ref. [6] Copyright 2023, Annual Reviews. C) In situ ATR-SEIRAS spectra of $Zn_1NC$-800, $Zn_1NC$-900, $Zn_1NC$, and $Zn_1NC$-1100 under different potentials in $CO_2RR$. The flow rate of the $CO_2$ inlet was 30 mL $min^{-1}$. Reproduced with permission. Ref. [71] Copyright 2024, Wiley-VCH. D) In situ ATR-FTIR spectra of Cu–SAs/HGDY record at a potential range from −0.7 to −1.5 V. Reproduced with permission. Ref. [72] Copyright 2023, Wiley-VCH. E) Potential-dependent ATR-FTIR spectra on $Fe_{NCs}/Fe_{SAs}$–NPC during $CO_2$ reduction in the 0.5 M $KHCO_3$ aqueous solution. Reproduced with permission. Ref. [73] Copyright 2024, Wiley-VCH.

 

of reaction intermediates in electrocatalytic experiments using ATR-fourier transform infrared spectroscopy (FTIR) to investigate the impact of the coordination environment of Cu active sites on the catalytic activity of $CO_2$RR. As illustrated in Figure 4D, two distinct IR peaks emerge at 1226 and 1480 $cm^{-1}$, corresponding to the intermediates $^*CHO$ and $^*OCH_2$, respectively, upon applying progressively negative potentials. These intermediates are essential in the pathway of $CO_2$RR toward $CH_4$ formation. In another study, He et al. prepared Fe single-atom materials loaded with N, P-codoped porous carbon, which can promote the activation of $CO_2$ molecules and accelerate $CO_2$RR kinetics.[73] The team used in situ ATR-FTIR to monitor the dynamic changes of adsorbed species on the catalyst surface. As shown in Figure 4E, for $CO_2$RR, a small positive peak was detected at 1410 $cm^{-1}$ within the voltage range of −0.2 to −0.9 V, corresponding to the adsorption of $^*COOH$.

To comprehensively elucidate the mechanism of $CO_2$RR on SACs, in situ IR can serve as a valuable tool for characterizing the atomically dispersed structures of the SACs and the reactants on their surfaces. By providing molecular-level insights into the dynamic interactions between SACs, intermediates, and reactants under operational conditions, in situ IR spectroscopy bridges the gap between catalyst structure and function. Specifically, in situ, IR can monitor the stretching of metal ligands to confirm atomic dispersion and distinguish SACs from nanoparticles/clusters. In addition, the drift of metal-ligand peaks under applied potential indicates structural evolution (such as ligand loss or aggregation).

For example, Zeng's group researched the configuration of adsorbed molecules on metal sites throughout the reaction process using in situ IR spectroscopy.[74] In the investigation of the $Cu-N_2O_2$ coordinated SAC Cu(OH)BTA for $CO_2$RR, a distinct IR absorption peak was identified at 2064–2019 $cm^{-1}$, as illustrated in **Figure 5A**, corresponding to vertically adsorbed CO ($^*CO_{atop}$) on the single Cu atom. When Cu(OH)BTA is subjected to a pre-electroreduction treatment, the $CO_2$RR reveals signals corresponding to bridge-adsorbed CO ($^*CO_{bridge}$) at neighboring Cu sites, specifically within the range of 1841–1820 $cm^{-1}$, in addition to this of $^*CO_{atop}$ (Figure 5B). This phenomenon is ascribed to the permanent formation of Cu clusters due to the electroreduction process. By analyzing the signals associated with various adsorption modes of CO in the in situ FT-IR spectra, one can infer the existing state of Cu within the SAC and its dynamic transformation processes. In another study, Yue et al. used in situ ATR-SEIRAS measurements to identify the intrinsic structure feature of single-Sn-atom sites on the $CO_2$RR performance.[75] As shown in Figure 5C,D, the peaks located at 1800–2000 $cm^{-1}$ over a wide potential range could be attributed to $^*CO$. A much higher $^*CO$ coverage over $P-SnN_4-CNT$ was observed compared to that of $SnN_4-CNT$, indicating that the presence of P promotes the activation of $CO_2$ and the dissociation of water, thereby accelerating the hydrogenation of $^*COOH$ to generate $^*CO$ and $H_2O$, which is responsible for the enhanced $CO_2$RR to CO over $P-SnN_4-CNT$.

Despite the substantial progress achieved in laboratory-based infrared spectroscopy, tracking the dynamic adsorption and desorption processes of surface molecules, typically occurring on picosecond timescales, continues to be a formidable challenge.[76,77] Fortunately, synchrotron radiation sources with pulse time resolutions up to the picosecond scale are particularly suitable for detecting transient intermediates. The schematic illustrating the operando synchrotron radiation characterization is shown in **Figure 6A**. Moreover, Synchrotron radiation-based sources have several advantages, including 2–3 orders of brightness, high fluxes, inherent polarization, and a broader frequency band spectrum, enabling enhanced surface sensitivity and more detailed molecular information.[78] As depicted in Figure 6B, in the mid-IR range, two predominant feature regions emerge: the fingerprint region, spanning 350–1500 $cm^{-1}$, and the functional group region, covering 1500–4000 $cm^{-1}$. Synchrotron radiation-based infrared (SR-IR) spectroscopy possesses distinct fingerprint characteristics and enhanced temporal resolution enabling qualitative or semi-quantitative sophisticated detail for identifying surface species on the electrochemical surface during $CO_2$RR. For example, Song's research team conducted operando synchrotron-radiation infrared absorption spectroscopy on a Ni–N–C catalyst, revealing a dual adsorption phenomenon of CO at Ni sites.[79] The elevated wavenumber associated with the double peaks represented for CO intermediates suggests the presence of higher valence $Ni^{\delta+}$ sites. Under negative potential, the two CO peaks exhibited distinct adsorption behaviors, indicating an asymmetric electronic structure of the $Ni^{\delta+}$ site (Figure 6C,D). The SR-IR characterization provides novel insights into the mechanisms underlying the efficient $CO_2$RR at these asymmetric $Ni^{\delta+}$ sites.

### 4.2. In Situ and Operando Raman Spectroscopy

Raman spectroscopy is grounded in the principle of inelastic light scattering induced by molecular vibrational modes. Upon interaction of a laser with molecules, a minor fraction of the scattered photons undergo energy shifts, thereby generating distinctive Raman spectra that serve as molecular fingerprints of the sample.[80] Similar to in situ infrared testing equipment, two compartments are separated by a Nafion membrane in the electrochemical Raman cell setup (**Figure 7A**).[6] To prevent the accumulation of hydrogen bubbles generated at negative potentials during the testing process, a $CO_2$-saturated electrolyte is continuously circulated through the working electrode channel. In situ Raman spectroscopy, a pivotal technique in the field of in situ vibrational spectroscopy, is capable of monitoring the surface structure of catalysts and the formation of intermediates during electrochemical processes in real-time.[81,82]

For example, Liu et al. designed a $Ni-N_4$ nickel single-atom catalyst (Ni SAC) bonded on a conductive carbon support and used operando Raman spectroscopy to monitor the state changes of Ni centers during the $CO_2$RR process.[31] As shown in Figure 7B,C, under an Ar atmosphere, a cathodic potential beyond −0.57 V (vs RHE) caused a shift in the Ni–N vibrational peak to lower wavenumbers, suggesting a weakening of the metal−nitrogen bond. Upon introducing $CO_2$ into the electrolyte, the Ni–N vibrational peak reverted to its original shape and energy position, remaining stable across the cathodic potential range from the open-circuit potential (OCP) to 0.37 V (vs RHE). These findings imply that Ni in NiTAPc undergoes reduction during the $CO_2$RR, with the in situ generated $Ni^+$ species demonstrating significant activity for $CO_2$ activation. Shen et al. prepared a single-atom Cu catalyst with second-shell sulfur coordination ($Cu-C_3N_4-S$),

 

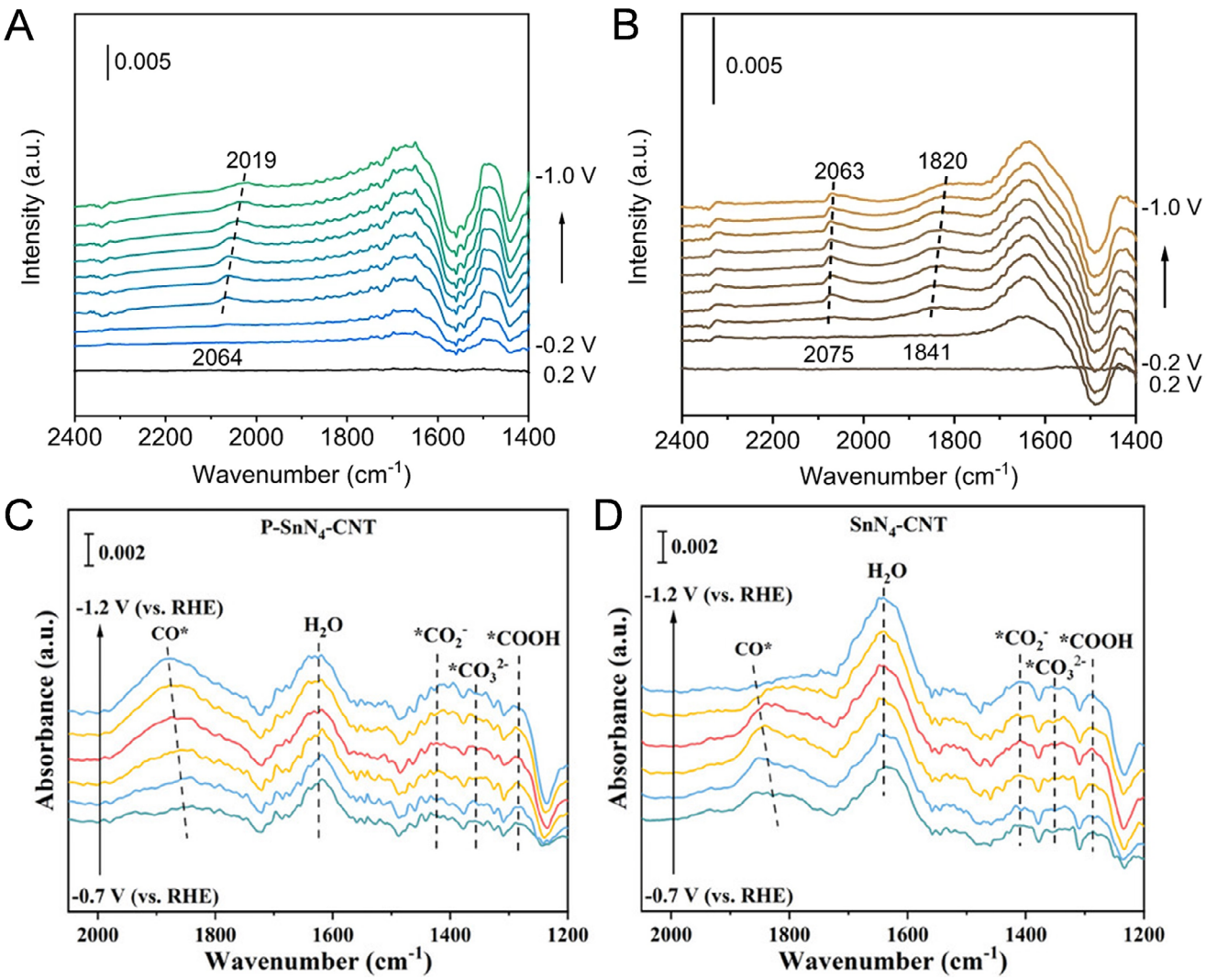


**Figure 5.** A) In situ ATR-SEIRAS spectra of Cu(OH)BTA in $CO_2$-saturated 0.1 M $KHCO_3$ electrolyte at the applied potential of −0.2 to −1.0 V. B) In situ ATR-SEIRAS spectra of $CO_2$RR on Cu(OH)BTA-derived Cu in $CO_2$-saturated 0.1 M $KHCO_3$ electrolyte. Reproduced with permission. Ref. [74] Copyright 2023, Springer Nature. In situ ATR-SEIRAS spectra of C) P-$SnN_4$-CNT and D) $SnN_4$-CNT in $CO_2$-saturated solution. Reproduced with permission. Ref. [75] Copyright 2024, Wiley-VCH.

exhibiting higher ethylene ($C_2H_4$) Faradaic efficiency.[83] To thoroughly examine the augmented $C_2H_4$ production process and investigate the fundamental mechanisms involved, in situ Raman spectroscopy was employed to observe and identify the intermediate's formation and adsorption (Figure 7D,E). Compared to the adsorption characteristics of intermediates on Cu−$C_3N_4$, a significant difference was noted for Cu−$C_3N_4$−S. Specifically, the peak intensity of $^*CO_2$ markedly elevated and displayed a blueshift as the reaction progressed. This observation suggests that Cu−$C_3N_4$−S demonstrates a greater selectivity for $^*CO_2$ adsorption relative to $^*H$, with increased adsorption of $CO_2$ evident throughout the course of the reaction.

The in situ Raman spectroscopy can gather information about adsorbate species and single-atom center state changes by capturing vibrational signals from both the adsorbates and other abundant atoms in the substrate.[84,85] Wu et al. used Ni−$N_4$ SACs to selectively detect the influence of cations such as $K^+$ on electrocatalytic $CO_2$RR and determine their interaction with chemisorbed $CO_2^-$.[86] As shown in Figure 7F, when the applied potential is −0.4 V, peak B corresponds to the C—O bond, while peak C is assigned to the asymmetric O–C–$O^-$ stretching mode. As the applied voltage shifts to a more negative region, peak C increases and peak B decreases. Similar situations did not occur in the experiment without adding cations. These experimental phenomena confirm that the chemically adsorbed $CO_2^-$ can exist stably in the presence of $K^+$. In another report by this research group, a layered double hollow spherical nanoreactor loaded with single-atom nickel was prepared, exhibiting excellent electrocatalytic $CO_2$RR performance.[49] In situ Raman spectroscopy and simulation calculations confirmed that the catalyst can effectively increase local CO concentration and limit CO release, ultimately enhancing C–C coupling (Figure 7G).

However, owing to the minimal loading of most SACs and the highly dispersive characteristics of the single-atom centers,

 

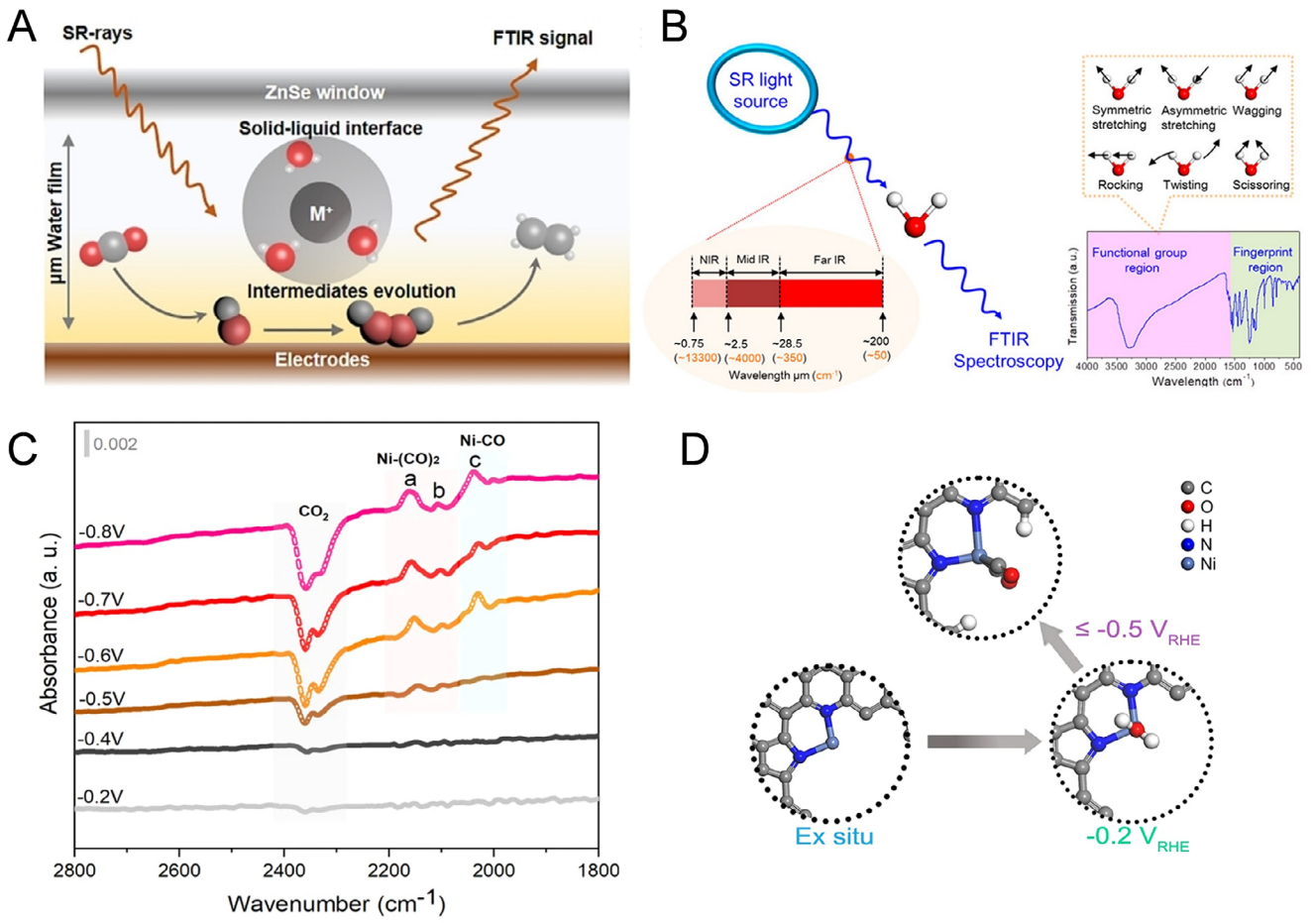


**Figure 6.** SR-IR for detecting surface adsorption molecules/intermediates and revealing reaction pathways. A) Schematic for correlative SR-FTIR spectroscopies; B) Schematic for SR-FTIR spectroscopy. Reproduced with permission. Ref. [78] Copyright 2022, American Chemical Society. C) SR-IRAS spectra were collected among −0.2 to −0.8 V (vs RHE) in 0.5 M $KHCO_3$. D) Schematic illustration of the potential-induced structure changes of low-valence Ni sites in Ni–N–C. Reproduced with permission. Ref. [79] Copyright 2023, Springer Nature.

Raman signals are generally weaker than infrared signals, which makes it exceedingly challenging to confirm reaction species by directly detecting the bonding vibrations between single-atom centers and adsorbates.[87] Surface-enhanced Raman spectroscopy (SERS) is a highly sensitive analytical technique that exploits the Raman scattering phenomenon. The signal enhancement in SERS is predominantly attributed to localized surface plasmon resonance (LSPR) occurring on the surfaces of noble metal nanostructures, such as gold (Au), silver (Ag), and copper (Cu). By engineering these nanostructures, SERS can significantly amplify Raman scattering signals, thereby facilitating its extensive application in trace detection, molecular identification, and interfacial surface analysis.[88] For instance, Han and colleagues developed a silica-mediated, hydrogen-bonded organic framework (HOF) templating strategy for the fabrication of high-density SACs featuring Cu–$N_3$ coordination site.[89] In situ, SERS was adopted in the electrochemical $CO_2$RR to explore the reaction mechanism. When applying potentials from −0.8 to −1.0 V (vs RHE), two characteristic Raman peaks were observed at 293 and 351 $cm^{-1}$, corresponding to the frustrated rotational mode of the C═O group and the stretching vibration of the Cu—CO bond, respectively (**Figure** 8A). As the potential was further increased to −1.3 V (vs RHE), the peak at 2010 $cm^{-1}$ shifted to 2042 $cm^{-1}$, attributed to the electrochemical Stark effect, reflecting the interaction between the external electric field and top-adsorbed CO species (Figure 8B). This spectral shift suggests that $CO^*$ species bound atop the Cu sites exhibit enhanced C–C coupling activity, thereby favoring the ethanol formation pathway.[90]

In addition, hell-isolated nanoparticle-enhanced Raman spectroscopy (SHINERS) has become a crucial tool in heterogeneous catalysis for characterizing complex structures. Li and colleagues developed a highly sensitive strategy for the structural characterization of SACs and real-time monitoring of catalytic reaction processes using SHINERS for the first time (Figure 8C).[91] As illustrated in Figure 8D,E, SHINERS was employed to track the nucleation and growth of Pd on $TiO_2$, revealing the transformation from single atoms (SAs) to nanoparticles (NPs). After 2.5 min of Pd nucleation, only a Raman band at 2129 $cm^{-1}$ was observed, corresponding to the linear adsorption of phenyl isocyanide (PIC) on Pd, indicative of isolated Pd single atoms. As nucleation progressed to 15 min, a new Raman band at 2028 $cm^{-1}$ emerged, corresponding to the bridge-bound PIC species, suggesting the coexistence of both Pd NPs and Pd SAs. With further extension of the nucleation time, the intensity of the bridge-bound

 

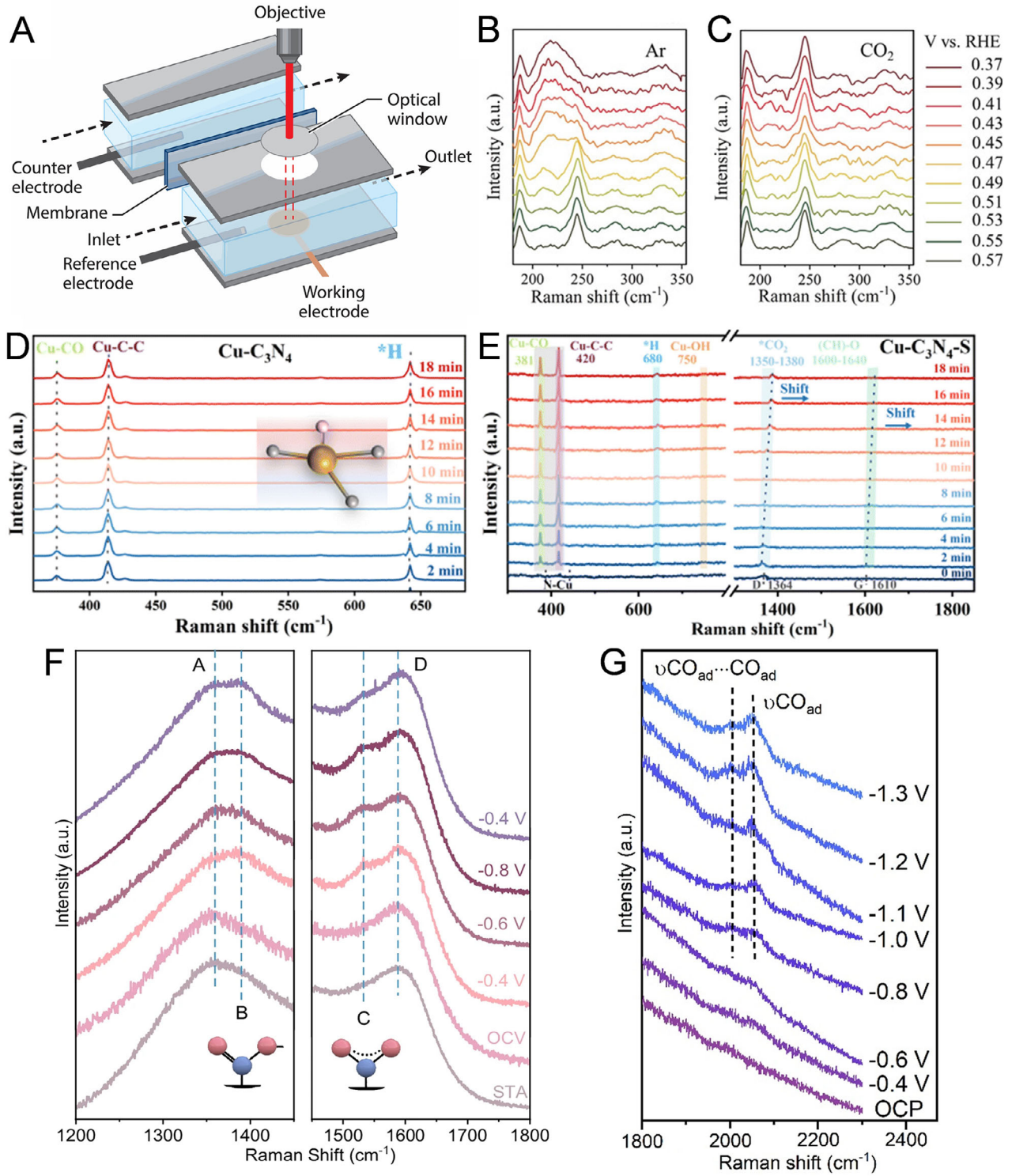


**Figure 7.** A) Schematic diagram of the electrochemical Raman cell design. Reproduced with permission. Ref. [6] Copyright 2023, Annual Reviews. B,C) Operando Raman spectra of Ni-TAPc collected on an Au electrode at various potentials (vs RHE) in 0.5 M $KHCO_3$ aqueous solution at room temperature under an atmosphere of (B) Ar (1 atm) and (C) $CO_2$ (1 atm). Reproduced with permission. Ref. [31] Copyright 2020, Wiley-VCH. D,E) In situ Raman spectra were collected at a time interval of 2 min under the $CO_2$RR conditions: (D) Cu–$C_3N_4$ from 350 to 690 $cm^{-1}$. (E) Cu–$C_3N_4$–S from 300 to 1850 $cm^{-1}$. Reproduced with permission. Ref. [83] Copyright 2024, Royal Society of Chemistry. F) In situ Raman spectra in $CO_2$-saturated 1 M KCl solution with a variation of applied potential. Reproduced with permission. Ref. [86] Copyright 2024, Springer Nature. G) In situ Raman spectra of Ni-SA@Cu-NP during the $CO_2$RR at different potentials in 1 M KOH at room temperature. Reproduced with permission. Ref. [49] Copyright 2024, American Chemical Society.

 

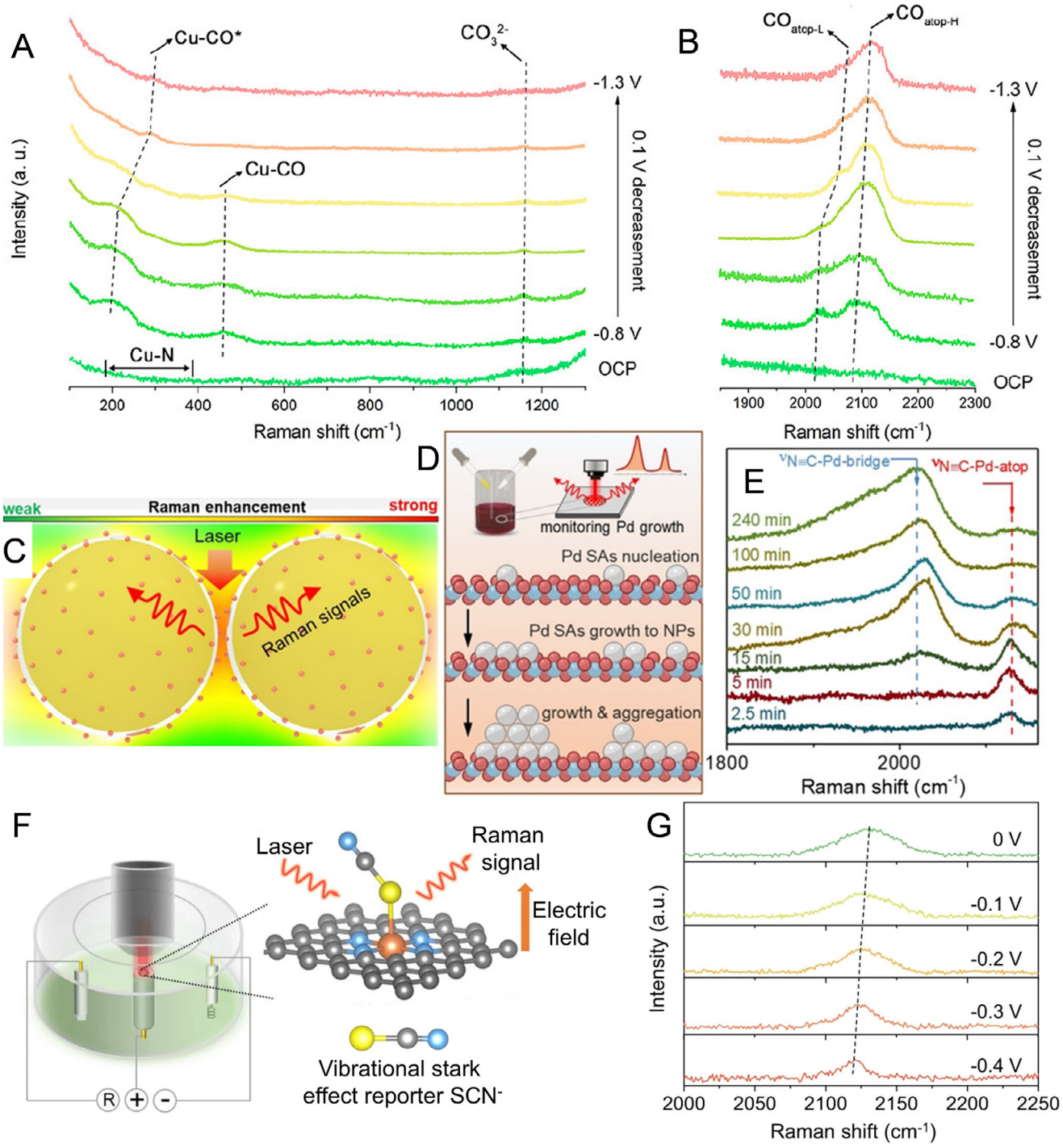


**Figure 8.** A,B) In situ electrochemical surface-enhanced Raman spectroscopy measurements during the $CO_2$RR. Reproduced with permission. Ref. [89] Copyright 2023, American Chemical Society. C) Raman enhancement of SHINERS-SACs-satellite nanocomposites. D,E) Illustration of Raman studies of the growth of Pd species from SAs to NPs. SHINERS spectra during the growth of Pd on Au@$TiO_2$. Reproduced with permission. Ref. [91] Copyright 2021, Wiley-VCH. F) Schematic diagram of probing the electric field of the active site in different-sized Ni-SACs by using the vibrational Stark effect. G) Potential-dependent SHINERS spectra of $SCN^-$ adsorbed on Ni-SAC-70 in 0.1 M $NaClO_4$ solution. Reproduced with permission. Ref. [92] Copyright 2024, Springer Nature.

 

PIC band increased, while that of the linearly adsorbed PIC decreased. These observations indicate that Pd initially forms as atomically dispersed species, which subsequently aggregate into nanoparticles over time. In another work, Lum et al. explored the effect of interfacial electric fields on electrocatalytic $CO_2$RR, using M–$N_4$ SACs supported on carbon nanospheres of varying diameters.[92] They utilized in situ SHINERS to investigate the relationship between the curvature of the spherical catalyst and the interfacial electric field (Figure 8F). $SCN^-$ was used as an electric field Stark shift probe due to its selective association with Ni single atoms, providing a direct measure of the interfacial electric field at the active sites. The study revealed that carbon nanospheres with greater curvature (i.e., smaller size) exhibited higher Stark tuning rates (Figure 8G), indicating stronger interfacial electric fields that enhance electrochemical performance by modifying the adsorption states and stability of reactants and intermediates.

### 4.3. In Situ and Operando X-Ray Absorption Spectroscopy

XAS employs synchrotron radiation to investigate the characteristics of a catalyst. The XAS spectrum is categorized into two distinct regions: XANES and EXAFS, based on their characteristics relative to the absorption edge.[93] The EXAFS region can extend several thousand electronvolts beyond the edge. The features observed in the XANES region are attributed to the transitions of electrons from occupied to unoccupied states, thereby providing insights into the oxidation state and electronic structure of the catalyst.[94] Generally, XANES is employed for qualitative analysis, while semi-quantitative analysis necessitates applying linear combination analysis. Following the edge, the interaction of the photoelectrons ejected by the adsorbed atoms with the electrostatic fields of adjacent atoms is translated into signal oscillations, which are observed in the EXAFS.[95] EXAFS exhibits a high sensitivity to the coordination environment, rendering it an effective technique for quantitatively assessing coordination numbers, bond lengths, and disorder factors.[96] A review addressing in situ XAS elaborates on the operational principles, challenges, and detection modalities associated with this methodology.[97] The in situ electrochemical XAS testing device is shown in **Figure 9A**.[98] The windows are transparent to X-rays and exhibit both corrosion resistance and impermeability. The thinner design minimizes the absorption of X-rays by the electrolyte, thereby ensuring the accurate acquisition of XAS data.

The activity and selectivity of $CO_2$RR are intrinsically tied to catalyst properties, including oxidation state, structural configuration, bond length, and coordination numbers.[99–101] To elucidate the nature of active sites and establish correlations among catalyst evolution, reaction kinetics, and product selectivity, in situ XAS has emerged as a critical tool. For example, alterations in the valence state change of the metal center are typically monitored using in situ XPS and in situ XAS (XANES) spectroscopy. Liu et al. utilized both in situ XPS and in situ XAS to investigate the evolution of catalysts during $CO_2$ reduction involving Ni SACs.[31] Their findings indicated that under cathodic bias in an Ar atmosphere, single Ni atoms transitioned from $Ni^{2+}$ to $Ni^+$ (Figure 9B,C), which were identified as the real active sites for activating $CO_2$ molecules via electrophilic addition. It is important to note that while in situ XPS can analyze the surface composition of catalysts, it may not provide comprehensive information regarding the changes in the valence states of metal centers. In contrast, in situ, XAS offers a more thorough assessment of these changes. Therefore, in situ, XAS is strongly favored for the monitoring of oxidation state variations in SAC. In a separate study, Chala et al. reported NiCu-SACs/N–C catalysts featuring cooperative dual heteroactive sites.[102] In-operando XAS and model-based fitting analysis reveal two key observations: the dynamic restructuring of Cu clusters derived from atomically dispersed Cu single atoms, and the reversible structural or oxidation state changes of Cu sites. In contrast, Ni sites remained unchanged throughout the catalytic process (Figure 9D–F).

A major challenge in advancing high-efficiency electrocatalysts for the electroreduction of $CO_2$ is the insufficient understanding of the chemical states and dynamic atomic configurations that evolve under potential-driven conditions. Chen's group utilized a synergistic approach that integrated in situ and operando methodologies, utilizing Cu SA electrocatalysts as a research model.[103] As shown in **Figure 10A**, the wavelet-transformed (WT) EXAFS spectra display a pronounced WT signal centered at an interatomic distance of 1.6 Å, suggesting that the Cu ions in the assynthesized N–Cu SAC are predominantly coordinated with N atoms and exhibit characteristics of single-atom behavior. Upon reaching a cathode potential of −0.8 V (vs RHE), alterations in the coordination environment surrounding the Cu site are observed. This change can be attributed to the emergence of a Cu–Cu scattering pathway, indicating the formation of copper clusters. In addition, quantitative analysis of in situ XANES and EXAFS spectra was performed through precise linear combinations (Figure 10B,C) to dynamically identify evidence of the evolving chemical state of the electrocatalyst.

In addition, Fang et al. loaded transition metal atoms (Fe, Co, Ni, Cu) onto nitrogen-doped carbon (M–N–C) to prepare a sequence of single-atom materials, which were used for electrocatalytic $CO_2$RR testing.[104] In situ XAS testing observed a decrease in the average coordination number of Ni at the voltage point with maximum Faraday efficiency, confirming the correlation between coordination number and catalytic performance. Wu et al. conducted in situ XANES experiments in $KHCO_3$ solution for real-time monitoring of the dynamic changes of single atom active centers during $CO_2$RR process,[86] The collected spectral evidence confirms that chemisorbed $CO_2^-$ and $K^+$ interactions adjust the rate-determining step, leading to an independent proton transfer mechanism.

Although in situ XAS can effectively reveal adsorbate alterations during electrochemical reactions by examining the coordination environment of the metal center. However, it is important to recognize that XAS spectra yield averaged coordination of metal atoms, which can complicate the difference between M—N and M—O coordination.[9] Many intermediates participating in electrochemical processes typically engage with the metal through M—N(O) bonding. This interaction frequently overlaps with the metal's bonding to the substrate, represented as M—$N(O)_x$, making it challenging to attribute changes in the coordination environment to either the adsorption of molecules or dynamic structural modifications of the metal itself.[105] Moreover, XAS exhibits heightened sensitivity to the first-shell

 

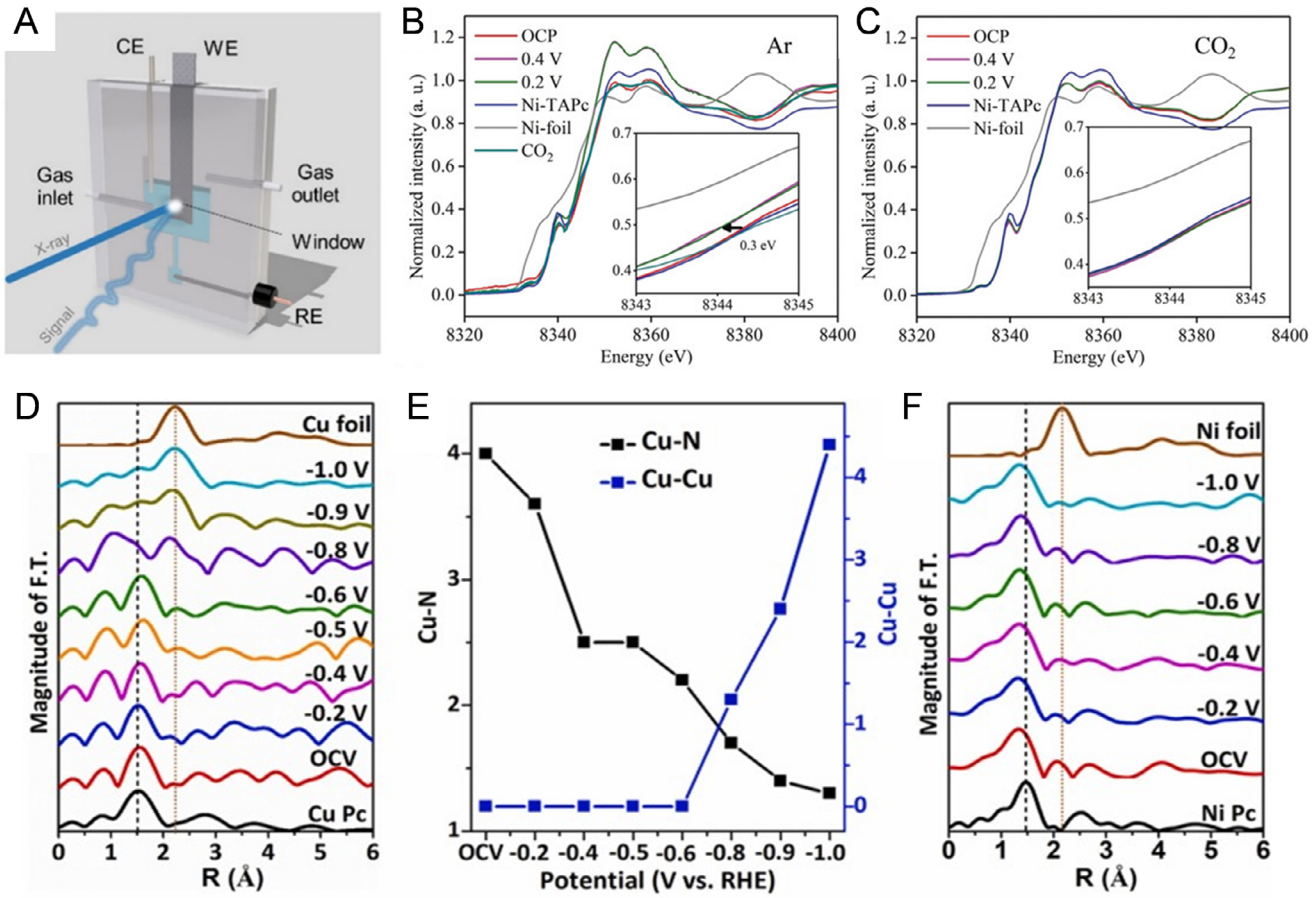


**Figure 9.** A) In situ XAS cell with fluorescence mode. Abbreviations: WE (working electrode), CE (counter electrode), and RE (reference electrode). The light blue liquid represents the electrolyte. Reproduced with permission. Ref. [98] Copyright 2024, American Chemical Society. B,C) Normalized Ni K-edge XANES spectra of Ni-CNT-CC acquired at various applied potentials (vs RHE) in 0.5 M $KHCO_3$ aqueous solution at room temperature under an atmosphere of (B) Ar (1 atm) and (C) $CO_2$ (1 atm); inset, enlarged Ni K-edge XANES. The OCP is about 0.57 V (vs RHE). The $CO_2$ line in (B) was obtained 5 min after switching Ar to $CO_2$ at 0.2 V (vs RHE). Reproduced with permission. Ref. [31] Copyright 2020, Wiley-VCH. D) The operando EXAFS spectra, E) the corresponding average coordination number for Cu–N and Cu–Cu shells of the Cu K-edge for 3% NiCu-SACs/N–C hybrid recorded during the $CO_2$ electrolysis at different applied potentials in $CO_2$-saturated 0.5 M $KHCO_3$ along with CuPc and Cu foil reference. F) The operando EXAFS spectra of Ni K-edge for 3% NiCu-SACs/N–C hybrid were recorded during the $CO_2$ electrolysis at different applied voltages along with NiPc and Ni foil reference. Reproduced with permission. Ref. [102] Copyright 2024, Elsevier.

coordinated atoms surrounding individual metal sites while offering limited information regarding atoms situated in the second or higher coordination shells that bond reaction intermediates with metal.[106] As a result, changes in the coordination environment of the metal center, as detected through in situ XAS, can yield valuable insights into the trends associated with changes in adsorbates; however, it is insufficient for the precise identification of the specific adsorbed species.

### 4.4. In Situ and Operando Transmission Electron Microscopy

Recent advancements in aberration-corrected TEM have allowed for investigating SACs with unprecedented detail. However, most of these investigations have been carried out under ultra-high vacuum conditions required by the electron microscope, thus limiting the research to ex situ analysis.[107] In contrast, the rapid development of in situ TEM over the past decades has sparked research into structural investigations under various external stimuli, including cooling, heating, and electric fields.[108,109] The study of SACs has been greatly advanced by developments in situ TEM, particularly through applying environmental TEM (ETEM), liquid electrochemical TEM (EC-TEM), and gas cell techniques, allowing catalysts to be studied in the gaseous and liquid environment. These novel techniques elucidate catalytic mechanisms at the atomic scale, which is pivotal for the design and optimization of SACs. A schematic representation of the electrochemical TEM setup and the associated electrochemical chip is shown in **Figure 11A**.

In the field of electrocatalytic $CO_2$RR applications, DeRitad et al. loaded atomically dispersed Pt onto $TiO_2$ nanoparticle (NP) support and characterized the materials under different redox states using in situ high-angle annular dark-field HAADF-STEM.[110] As shown in Figure 11B, the isolated Pt possesses the ability to undergo evolutionary changes in response to variations in environmental conditions, allowing it to adapt to diverse

 

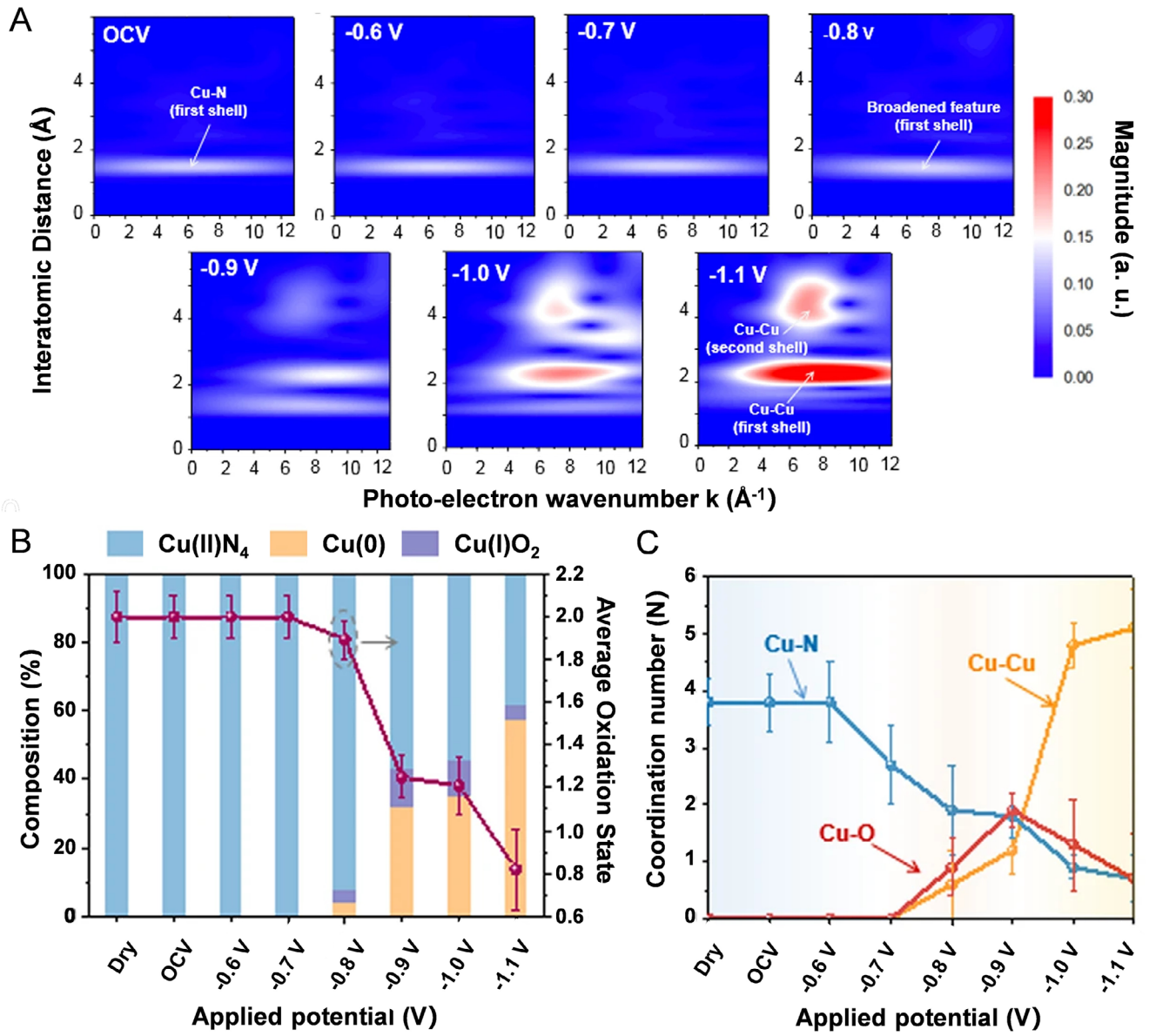


**Figure 10.** A) Wavelet-transform diagram of in situ Cu K-edge EXAFS spectra of N–Cu SAC at various applied potentials in $CO_2$-saturated 0.1 M $KHCO_3$ solution during $CO_2$ reduction. B) Extracted oxidation state from in situ Cu K-edge XANES of N–Cu SAC spectra through a linear combination of Cu foil, $Cu_2O$, and $Cu(bipy)_4Cl$ as spectroscopic references in $CO_2$-saturated 0.1 M $KHCO_3$ solution. C) Quantitative analysis of coordination environment extracted from EXAFS fitting at various potentials in $CO_2$-saturated 0.1 M $KHCO_3$ solution. Error bars represent the standard deviation of three independent measurements. Adapted with permission. Ref. [103] Copyright 2023, Springer Nature.

local coordination environments and oxidation states. Besides, in situ STEM experiments and line-scan intensity analysis conducted over time indicate that the electron beam induces Pt motion under intense reducing conditions (Figure 11C). In another work, Hsu et al. prepared N–Cu SAC through the pyrolysis of a composite comprising 1-alanine, melamine, and copper acetate monohydrate.[103] This study successfully facilitated the direct observation of catalyst behavior under potential driven conditions. As shown in Figures 11D–F, liquid EC-TEM was employed to monitor the dynamic structural transformations of the Cu SAC electrocatalyst during the process of $CO_2$ reduction. After 80 s of electrolysis, two distinct spots, highlighted in orange and measuring ≈2.6 nm in diameter, emerged, indicating a restructuring process and the formation of clusters. Importantly, as denoted by the blue circles in Figure 11D, these clusters appear to exhibit the ability to migrate freely across the carbon support. In addition, Zhang et al. presented a single-atom catalyst composed of silver ($Ag_1/MnO_2$), synthesized via thermal transformation of Ag NPs and surface reconstruction of $MnO_2$.[111] The transition of Ag NPs into single atoms is elucidated for the first time using various techniques, including in situ TEM and in situ XRD. The resulting $Ag_1/MnO_2$ catalyst demonstrated a Faradaic efficiency of 95.7% at a potential of −0.85 V (vs RHE), alongside sustained stability for the electrochemical reduction of $CO_2$.

 

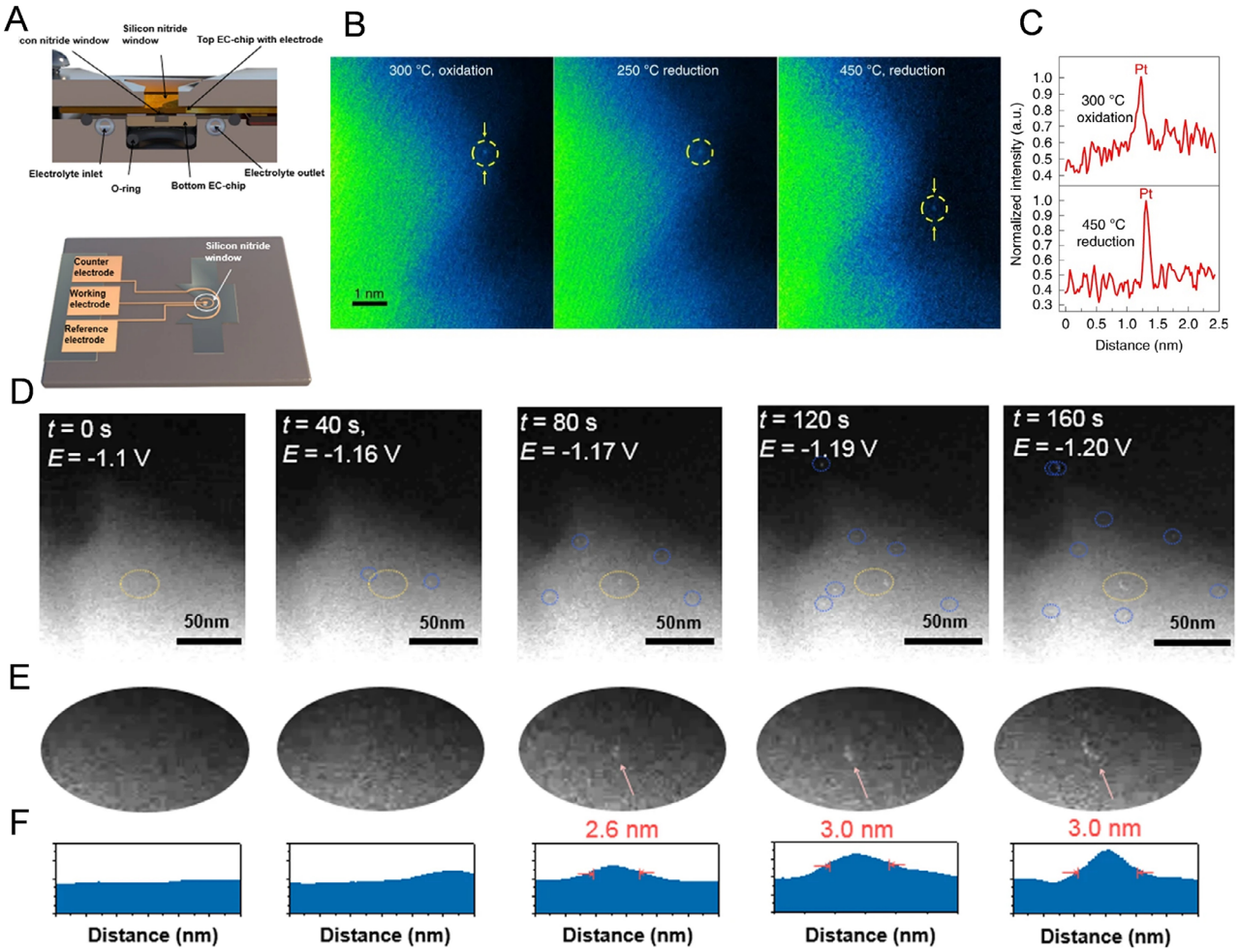


**Figure 11.** A) Schematic of in situ electrochemical TEM and corresponding electrochemical chip. Reproduced with permission. Ref. [103] Copyright 2023, Springer Nature. B) In situ HAADF-STEM images of $Pt_{iso}/TiO_2$ after 30 min at different annealing conditions: 300 °C, 760 torr of $O_2$ for 30 min; 250 °C, 760 torr of 5% $H_2$ (balanced with Ar) for 30 min; 450 °C, 760 torr of 5% $H_2$ (balanced with Ar) for 30 min. C) The intensity profile of a line scan (along the yellow arrows) shown in A is normalized to the identified Pt atom. Reproduced with permission. Ref. [110] Copyright 2019, Springer Nature. Structural characterization of the as-prepared N–Cu SAC during $CO_2$RR: D) Dark-field STEM images at truly calibrated potentials versus RHE with various durations from 0 to 160 s. E) Magnified images of the selected area in (D). F) Line profiles of selected clusters. Reproduced with permission. Ref. [103] Copyright 2023, Springer Nature.

## 5. Summary and Perspective

In this review, we systematically summarized the SACs applied to $CO_2$RR and the in situ and operando characterization techniques involved in studying catalytic kinetics. Through a comprehensive review of research in this field in recent years, this article provides a detailed introduction to the technical features and characterization benefits of various technologies and further compares the advantages, limitations, and complementarity aspects of these technologies. Despite these advancements, fully understanding the dynamic reaction mechanisms of SACs in $CO_2$RR remains a significant challenge owing to the current limitations. The following sections will outline the key challenges and propose future research directions (**Figure 12**).

1) As previously discussed, the dynamic structural transformations of the SACs and the molecular activation/deactivation mechanisms at the gas-liquid-solid interface during CO2RR operation is highly intricate. The presence of liquid layers and gas bubbles at the gas-liquid-solid interface diminishes the concentration of the active centers and complicates signal detection. Consequently, there is an urgent need to explore novel possibilities within contemporary in situ and operando analytical techniques to decipher the dynamic structure of the three-phase interface accurately.
2) During in situ and operando testing, increased beam brightness and radiation-induced damage can lead to distortions in the electronic or geometric structure of the sample, and the SAC can encounter challenges like atomic agglomeration and reduced material activity. Additionally, dynamic transformations of interfacial active sites and molecular adsorption and desorption processes typically occur on timescales ranging from milliseconds to picoseconds. Therefore, time-resolved X-ray spectroscopy should be developed to more accurately

 

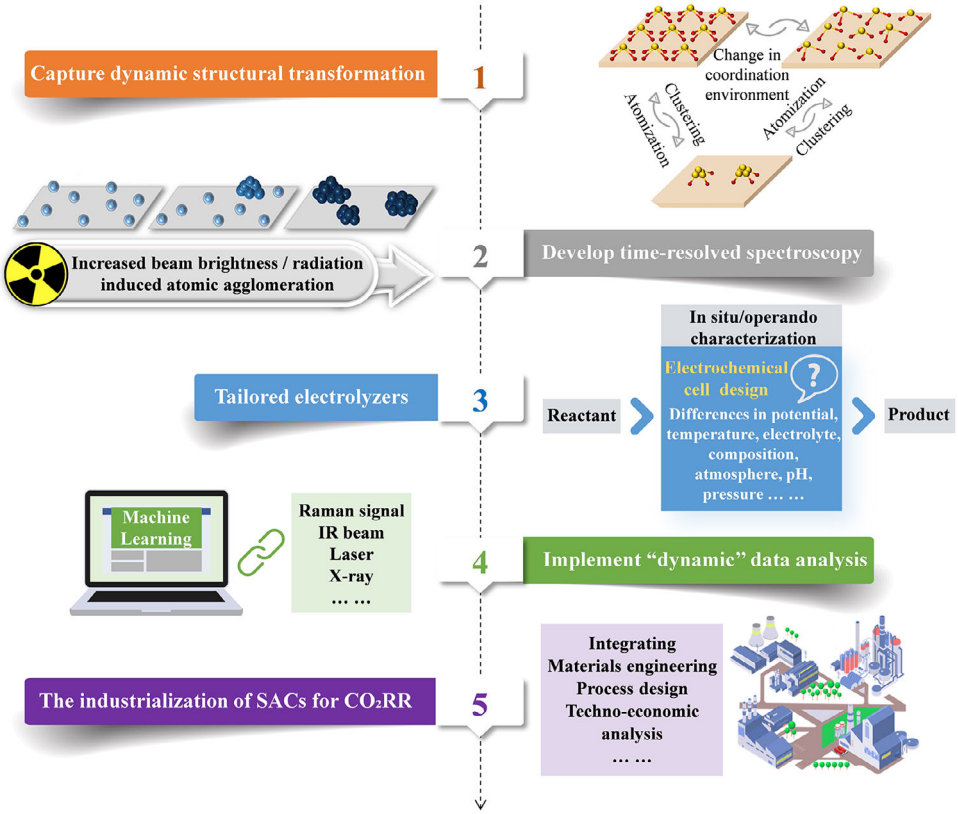


**Figure 12.** Illustration of future research perspectives in in situ and operando analytical techniques of SACs. Five prioritized directions: 1) capture dynamic structural transformation, 2) develop time-resolved spectroscopy, 3) tailored electrolyzers, 4) implement "dynamic" data analysis and 5) the industrialization of SACs for $CO_2$RR.

align detection results with the actual reaction, enabling real-time monitoring of dynamic evolution and elucidating the intrinsic relationship between structure, intermediates, and reaction activity.

3) As a vital element of the entire reaction system, the influence of electrochemical cells on the reaction process cannot be underestimated in CO2RR. It is essential to design a modular electrolytic cell system that is compatible with multiple characterization techniques, featuring interchangeable windows/electrodes suitable for X-ray, neutron, and optical probes. Furthermore, it is advisable to establish benchmark protocols for potential scanning rates, electrolyte flow parameters, and gas diffusion layer configurations. Such a framework will significantly improve cross-technology comparability and reproducibility.
4) Acquiring high-quality in situ and operando spectral data for SACs remains technically challenging due to signal-to-noise constraints and transient intermediate states under operational conditions. With the continuous advancement of technology, machine learning (ML) enables "dynamic" data analysis. Neural networks pre-trained on multi-scale spectral datasets can perform ultrafast (<1 s) analysis during experiments.
5) The industrialization of SACs for $CO_2$RR necessitates overcoming critical challenges, including scalable synthesis with atomic precision, and stability under industrial current densities (>100 mA $cm^{-2}$). Second, system-level integration must address $CO_2$ feedstock purity (e.g., dilute $CO_2$ from flue gas vs direct air capture), product separation, and energy consumption optimization in flow reactors. These challenges necessitate interdisciplinary approaches integrating materials engineering, process design, and techno-economic analysis to enable viable large-scale implementation.

In conclusion, despite existing challenges, the outlook for in situ and operando analysis techniques in characterizing SACs for $CO_2$RR is highly promising. As $CO_2$ electrolysis continues to gain traction as a significant research area, it is anticipated to drive extensive investigations focused on developing high-performance catalysts and elucidating future reaction mechanisms.

## Acknowledgements

R.S., X.L., and J.H. contributed equally to this work. This work was supported by grants from the National Natural Science Foundation of China (22405228, 22479163), the GuangDong Basic and Applied Basic Research Foundation (No. 2023A1515110259, 2025A1515011951), and the Strategic Hiring Scheme (BDD3) and Research Centre for Carbon-Strategic Catalysis (CE01) of The Hong Kong Polytechnic University.

## Conflict of Interest

The authors declare no conflict of interest.

 

## Author Contributions

R.S., Y.L., and J.G. prepared the manuscript. R.S., X.L., J.H., Y.W., and H.H. revised the manuscript. Y.L. and J.G. designed and revised the manuscript. All authors contributed to the discussion and preparation of the manuscript.

## Keywords

Electrocatalytic $CO_2$RR, In Situ and Operando characterization, single-atom catalysts

Received: March 13, 2025
Revised: May 11, 2025
Published online: June 13, 2025

[1] Z. Wang, L. Xu, Y. Zhou, Y. Liang, J. Yang, D. Wu, S. Zhang, X. Han, X. Shi, J. Li, Y. Yuan, P. Deng, X. Tian, *Chem. Soc. Rev.* **2024**, *53*, 6295.
[2] M. Jiang, H. Wang, M. Zhu, X. Luo, Y. He, M. Wang, C. Wu, L. Zhang, X. Li, X. Liao, Z. Jiang, Z. Jin, *Chem. Soc. Rev.* **2024**, *53*, 5149.
[3] R. Jin, Q. Wu, H. He, C. Wang, Y. Li, D. Jin, S. Liang, H. Ma, D. Li, R. Wang, Y. Li, X. Zhang, *Small Methods* **2025**, *9*, 2401704.
[4] H. Wang, R. Sun, P. Liu, H. Hu, C. Ling, X. Han, Y. Shi, X. Zheng, G. Wu, X. Hong, *Nano Res.* **2024**, *17*, 7013.
[5] X. Zhao, Q. Feng, M. Liu, Y. Wang, W. Liu, D. Deng, J. Jiang, X. Zheng, L. Zhan, J. Wang, H. Zheng, Y. Bai, Y. Chen, X. Xiong, Y. Lei, *ACS Nano* **2024**, *18*, 9678.
[6] B. Hasa, Y. Zhao, F. Jiao, *Annu. Rev. Chem. Biomol. Eng.* **2023**, *14*, 165.
[7] Z. Lang, X. Wang, S. Jabeen, Y. Cheng, N. Liu, Z. Liu, T. Gan, Z. Zhuang, H. Li, D. Wang, *Adv. Mater.* **2025**, *9*, 2418942.
[8] T. Wang, J. Chen, X. Ren, J. Zhang, J. Ding, Y. Liu, K. Hui, J. Wang, X. Li, H. Yang, Y. Huang, S. Kawi, B. Liu, *Angew. Chem., Int. Ed.* **2023**, *10*, 202211174.
[9] M. Liu, Y. Wang, T. Yu, L. Zhan, X. Zhao, C. Lian, Y. Xiong, X. Xiong, Y. Lei, *Sci. Bull.* **2023**, *68*, 1238.
[10] J. Jang, S. Zhu, E. P. Delmo, T. Li, Q. Zhao, Y. Wang, L. Zhang, H. Huang, J. Ge, M. Shao, *EcoMat* **2023**, *5*, 12334.
[11] Y. Liu, X. Su, J. Ding, J. Zhou, Z. Liu, X. Wei, H. B. Yang, B. Liu, *Chem. Soc. Rev.* **2024**, *53*, 11850.
[12] Y. Bai, D. Deng, J. Wang, Y. Wang, Y. Chen, H. Zheng, M. Liu, X. Zheng, J. Jiang, H. Zheng, M. Yi, W. Li, G. Fang, D. Wang, Y. Lei, *Adv. Mater.* **2024**, *36*, 2411404.
[13] S. Wang, L. Wang, D. Wang, Y. Li, *Energy Environ. Sci.* **2023**, *16*, 2759.
[14] Y. Li, H. Wang, X. Yang, T. O'Carroll, G. Wu, *Angew. Chem., Int. Ed.* **2024**, *63*, 202317884.
[15] Y. Wang, Q. Wang, J. Wu, X. Zhao, Y. Xiong, F. Luo, Y. Lei, *Nano Energy* **2022**, *103*, 107815.
[16] S. W. Jo, J. Y. Kim, M. W. Lee, Y. Kim, H. S. Ahn, *ACS Catal.* **2023**, *13*, 5122.
[17] W. Sun, S. Liu, H. Sun, H. Hu, J. Li, L. Wei, Z. Tian, Q. Chen, J. Su, L. Chen, *Adv. Energy Mater.* **2025**, *3*, 2500283.
[18] W. Zhang, D. Liu, T. Liu, C. Ding, T. Chen, Y. Li, X. Liu, L. Wang, C. Li, J. He, T. Ding, T. Yao, *Nano Res.* **2023**, *16*, 10873.
[19] H. Sun, Q. Liu, Z. Gao, L. Geng, Y. Li, F. Zhang, J. Yan, Y. Gao, K. Suenaga, L. Zhang, Y. Tang, J. Huang, *J. Mater. Chem. A* **2022**, *10*, 6096.
[20] B. Sun, X. Wang, Z. Li, H. Liu, W. Jiang, K. Song, Z. Wang, P. Wang, Y. Liu, Z. Zheng, Y. Dai, B. Huang, H. Cheng, *Chem Catal.* **2023**, *4*, 100862.
[21] D. Zhang, X. Liu, Y. Zhao, H. Zhang, A. V. Rudnev, J.-F. Li, *Chem. Sci.* **2025**, *16*, 4916.
[22] J. Han, X. Bai, X. Xu, X. Bai, A. Husile, S. Zhang, L. Qi, J. Guan, *Chem. Sci.* **2024**, *15*, 7870.
[23] X. Nie, M. R. Esopi, M. J. Janik, A. Asthagiri, *Angew. Chem., Int. Ed.* **2013**, *52*, 2459.
[24] J. H. Montoya, A. A. Peterson, J. K. Nørskov, *ChemCatChem* **2013**, *5*, 737.
[25] S. Vijay, W. Ju, S. Bru¨ckner, S. C. Tsang, P. Strasser, K. Chan, *Nat. Catal.* **2021**, *4*, 1024.
[26] C. Chen, J. Li, X. Tan, Y. Zhang, Y. Li, C. He, Z. Xu, C. Zhang, C. Chen, *EES Catal.* **2024**, *2*, 71.
[27] W. Ju, A. Bagger, G. P. Hao, A. Varela, I. Sinev, V. Bon, B. Cuenya, S. Kaskel, J. Rossmeisl, P. Strasser, *Nat. Commun.* **2017**, *8*, 944.
[28] T. K. Todorova, M. W. Schreiber, M. Fontecave, *ACS Catal.* **2019**, *10*, 1754.
[29] R. Kortlever, J. Shen, K. J. P Schouten, F. Calle-Vallejo, M. T. M. Koper, *J. Phys. Chem. Lett.* **2015**, *6*, 4073.
[30] A. A. Peterson, F. Abild-Pedersen, F. Studt, J. Rossmeisl, J. K. Nørskov, *Energy Environ. Sci.* **2010**, *3*, 1311.
[31] S. Liu, H. B. Yang, S.-F. Hung, J. Ding, W. Cai, L. Liu, J. Gao, X. Li, X. Ren, Z. Kuang, Y. Huang, T. Zhang, B. Liu, *Angew. Chem., Int. Ed.* **2020**, *59*, 798.
[32] J.-H. Liu, X. Cao, R. Wang, X. Chen, Y. Wang, P. Yang, J. Long, X. Yin, Z. Huang, D. Cao, *Sci. China Mater.* **2023**, *66*, 2741.
[33] Z. Jiang, T. Wang, J. Pei, H. Shang, D. Zhou, H. Li, J. Dong, Y. Wang, R. Cao, Z. Zhuang, W. Chen, D. Wang, J. Zhang, Y. Li, *Energy Environ. Sci.* **2020**, *13*, 2856.
[34] Y. Qiao, W. Lai, K. Huang, T. Yu, Q. Wang, L. Gao, Z. Yang, Z. Ma, T. Sun, M. Liu, C. Lian, H. Huang, *ACS Catal.* **2022**, *12*, 2357.
[35] Z. Pan, K. Wang, K. Ye, Y. Wang, H.-Y. Su, B. Hu, J. Xiao, T. Yu, Y. Wang, S. Song, *ACS Catal.* **2020**, *10*, 3871.
[36] T. Yan, X. Chen, L. Kumari, J. Lin, M. Li, Q. Fan, H. Chi, T. J. Meyer, S. Zhang, X. Ma, *Chem. Rev.* **2023**, *17*, 10530.
[37] J. Rosen, G. S. Hutchings, Q. Lu, S. Rivera, Y. Zhou, D. G. Vlachos, F. Jiao, *ACS Catal.* **2015**, *5*, 4293.
[38] Q. Zhang, J. Wang, F. Guo, G. He, X. Yang, W. Li, J. Xu, Z. Yin, *J. Energy Chem.* **2023**, *84*, 321.
[39] Y. Li, W. Shan, M. J. Zachman, M. Wang, S. Hwang, H. Tabassum, J. Yang, X. Yang, S. Karakalos, Z. Feng, G. Wang, G. Wu, *Angew. Chem., Int. Ed.* **2022**, *61*, 202205632.
[40] K. Liu, Z. Sun, W. Chen, X. Lang, X. Gao, P. Chen, *Adv. Funct. Mater.* **2024**, *34*, 2312589.
[41] K. Zhao, X. Nie, H. Wang, S. Chen, X. Quan, H. Yu, W. Choi, G. Zhang, B. Kim, J. G. Chen, *Nat. Commun.* **2020**, *11*, 2455.
[42] P. Shao, W. Zhou, Q.-L. Hong, L. Yi, L. Zheng, W. Wang, H.-X. Zhang, H. Zhang, J. Zhang, *Angew. Chem., Int. Ed.* **2021**, *60*, 16687.
[43] Y. Ying, X. Luo, J. Qiao, H. Huang, *Adv. Funct. Mater.* **2020**, *31*, 2007423.
[44] H. T. Chung, D. A. Cullen, D. Higgins, B. T. Sneed, E. F. Holby, K. L. More, P. Zelenay, *Science* **2017**, *357*, 479.
[45] Z. Xu, J. Mao, B. Mei, S. Gu, J. Ma, F. Sun, J. Li, L. Wang, W. Chen, F. Song, Z. Jiang, *Sci. China Chem.* **2025**, *68*, 2044.
[46] R. Chen, J. Zhao, X. Zhang, Q. Zhao, Y. Li, Y. Cui, M. Zhong, J. Wang, X. Li, Y. Huang, B. Liu, *J. Am. Chem. Soc.* **2024**, *146*, 24368.
[47] T. Zhao, B. Niu, W. An, B. Li, G. Li, Z. Shui, X. Duan, Z. Zhang, J. Cheng, Z. Hao, *Appl. Catal. B: Environ.* **2025**, *371*, 125277.
[48] L. Cheng, D. He, X. Ma, H. Deng, Y. Ruan, R. Sun, L. Tian, H. Zhou, J. Chen, X. Wang, H. Pan, W. Guo, Y. Wu, *Adv. Funct. Mater.* **2024**, *34*, 2406056.
[49] J. Song, H. Zhang, R. Sun, P. Liu, X. Ma, C. Chen, W. Guo, X. Zheng, H. Zhou, Y. Gao, W. Cui, H. Pan, Z. Zhang, Y. Wu, *ACS Nano* **2024**, *17*, 11416.
[50] S. Xue, X. Liang, Q. Zhang, X. Ren, L. Gao, O. Ma, A. Liu, *Catalysts* **2024**, *14*, 7.

 

[51] C. Zhu, Y. Song, X. Dong, G. Li, A. Chen, W. Chen, G. Wu, S. Li, W. Wei, Y. Sun, *Energy Environ. Sci.* **2022**, *15*, 5391.
[52] C. Kim, J. C. Bui, X. Luo, J. K. Cooper, A. Kusoglu, A. Z. Weber, A. T. Bell, *Nat. Energy* **2021**, *6*, 1026.
[53] Z.-Y. Song, P.-H. Li, Y.-Y. Li, M. Yang, J.-Y. Lin, B.-P. Xiong, R.-Z. Xia, X. Cai, W. Duan, S.-H. Chen, L. Li, W.-Q. Liu, X.-J. Huang, *Nano Lett.* **2025**, *25*, 3947.
[54] Y. Lin, B. Geng, R. Zheng, W. Chen, J. Zhao, H. Liu, Z. Qi, Z. Yu, K. Xu, X. Liu, L. Yang, L. Shan, L. Song, *Nat. Commun.* **2025**, *16*, 286.
[55] Z. Li, *Small Methods* **2024**, *8*, 2400478.
[56] A. Brennhagen, C. Cavallo, D. S. Wragg, J. Sottmann, A. Y. Koposov, H. Fjellvåg, *Batteries Supercaps* **2021**, *7*, 1039.
[57] Y. Gong, T. He, *Small Methods* **2023**, *7*, 2300702.
[58] Y. Yang, C. Shi, J. Feijóo, J. Jin, C. Chen, Y. Han, P. Yang, *J. Am. Chem. Soc.* **2024**, *146*, 23398.
[59] N. Schlüter, P. Novák, D. Schröder, *Adv. Energy Mater.* **2022**, *12*, 2200708.
[60] D. Mendoza, S. T. Dong, B. Lassalle-Kaiser, *Curr. Opin. Colloid Interface Sci.* **2022**, *61*, 101635.
[61] A. S. Malkani, J. Li, N. J. Oliveira, M. He, X. Chang, B. Xu, Q. Lu, *Sci. Adv.* **2020**, *6*, abd2569.
[62] Y. Zhao, X. Chang, A. S. Malkani, X. Yang, L. Thompson, F. Jiao, B. Xu, *J. Am. Chem. Soc.* **2020**, *142*, 9735.
[63] S. Soodi, J.-J. Zhang, J. Zhang, Y. Liu, M. Lashgari, S. Zafeiratos, A. Züttel, K. Zhao, W. Luo, *Chem. Synth.* **2024**, *4*, 44.
[64] R. M. Arán-Ais, R. Rizo, P. Grosse, G. Algara-Siller, K. Dembélé, M. Plodinec, T. Lunkenbein, S. W. Chee, B. R. Cuenya, *Nat. Commun.* **2020**, *11*, 3489.
[65] Z. Mu, N. Han, D. Xu, B. Tian, F. Wang, Y. Wang, Y. Sun, C. Liu, P. Zhang, X. Wu, Y. Li, M. Ding, *Nat. Commun.* **2022**, *13*, 6911.
[66] J. Disch, L. Bohn, S. Koch, M. Schulz, Y. Han, A. Tengattini, L. Helfen, M. Breitwieser, S. Vierrath, *Nat. Commun.* **2022**, *13*, 6099.
[67] Z. Liu, Y. Liu, J. Zhang, T. Cao, Z. Sun, J. Liu, H. Shang, *Nano Res.* **2024**, *17*, 3911.
[68] N. Cao, N. Zhang, K. Wang, K. Yan, P. Xie, *Chem. Synth.* **2023**, *3*, 23.
[69] G. Wang, X. Ke, M. Sui, *Chem. Res. Chin. Univ.* **2022**, *38*, 1172.
[70] E. P. Delmo, Y. Wang, Y. Song, S. Zhu, H. Zhang, H. Xu, T. Li, J. Jang, Y. Kwon, Y. Wang, M. Shao, *J. Am. Chem. Soc.* **2024**, *146*, 1935.
[71] Q. Hao, C. Zhen, Q. Tang, J. Wang, P. Ma, J. Wu, T. Wang, D. Liu, L. Xie, X. Liu, M. D. Gu, M. R. Hoffmann, G. Yu, K. Liu, J. Lu, *Adv. Mater.* **2024**, *36*, 2406380.
[72] P. Zhao, H. Jiang, H. Shen, S. Yang, R. Gao, Y. Guo, Q. Zhang, H. Zhang, *Angew. Chem., Int. Ed.* **2023**, *62*, 202314121.
[73] J. He, L. Xu, C. Qin, J. Zhang, D. Liu, Q. Li, Z. Feng, J. Wang, P. Liu, H. Li, Z. Yang, *Small* **2024**, *20*, 2405157.
[74] Y. Liang, J. Zhao, Y. Yang, S.-F. Hung, J. Li, S. Zhang, Y. Zhao, A. Zhang, C. Wang, D. Appadoo, L. Zhang, Z. Geng, F. Li, J. Zeng, *Nat. Commun.* **2023**, *14*, 474.
[75] C. Yue, X. Yang, X. Zhang, S. Wang, W. Xu, R. Chen, J. Wang, J. Yin, Y. Huang, X. Li, *Adv. Energy Mater.* **2024**, 2401448.
[76] E. R. Corson, R. Kas, R. Kostecki, J. J. Urban, W. A. Smith, B. D. McCloskey, R. Kortlever, *J. Am. Chem. Soc.* **2020**, *142*, 11750.
[77] C. M. Gunathunge, J. Y. Li, X. Li, J. J. Hong, M. M. Waegele, *ACS Catal.* **2020**, *10*, 6908.
[78] W. Cheng, H. Su, Q. Liu, *Acc. Chem. Res.* **2022**, *55*, 1949.
[79] Y. Zhou, Q. Zhou, H. Liu, W. Xu, Z. Wang, S. Qiao, H. Ding, D. Chen, J. Zhu, Z. Qi, X. Wu, Q. He, L. Song, *Nat. Commun.* **2023**, *14*, 3776.
[80] Y. Luo, S. Sheng, M. Pisarra, A. Martin-Jimenez, F. Martin, K. Kern, M. Garg, *Nat. Commun.* **2024**, *15*, 6983.
[81] T. Xie, S. Chen, Y. Yue, T. Sheng, N. Huang, Y. Xiong, *Angew. Chem., Int. Ed.* **2024**, *7*, 202411188.
[82] H. Shang, T. Wang, J. Pei, Z. Jiang, D. Zhou, Y. Wang, H. Li, J. Dong, Z. Zhuang, W. Chen, D. Wang, J. Zhang, Y. Li, *Angew. Chem., Int. Ed.* **2020**, *59*, 22465.
[83] Y. Shen, Y. Pan, H. Xiao, H. Zhang, C. Zhu, Q. Fang, Y. Li, L. Lu, L. Ye, S. Song, *J. Mater. Chem. A* **2024**, *12*, 9075.
[84] Y. Zhao, X.-G. Zhang, N. Bodappa, W.-M. Yang, Q. Liang, P. M. Radjenovica, Y.-H. Wang, Y.-J. Zhang, J.-C. Dong, Z.-Q. Tian, J.-F. Li, *Energy Environ. Sci.* **2022**, *15*, 3968.
[85] Y. Wang, Q. Li, M. Wang, H. Ou, D. Deng, H. Zheng, Y. Bai, L. Zheng, Z.-Y. Chen, W. Li, G. Fang, Y. Lei, *Nano Lett.* **2024**, *24*, 13653.
[86] F. Wu, X. Liu, S. Wang, L. Hu, S. Kunze, Z. Xue, Z. Shen, Y. Yang, X. Wang, M. Fan, H. Pan, X. Gao, T. Yao, Y. Wu, *Nat. Commun.* **2024**, *15*, 6972.
[87] Y. Zhao, L. Du, H. Li, W. Xie, J. Chen, *J. Phys. Chem. Lett.* **2019**, *10*, 1286.
[88] J. Yi, E.-M. You, R. Hu, D.-Y. Wu, G.-K. Liu, Z.-L. Yang, H. Zhang, Y. Gu, Y.-H. Wang, X. Wang, H. Ma, Y. Yang, J.-Y. Liu, F. R. Fan, C. Zhan, J.-H. Tian, Y. Qiao, H. Wang, S.-H. Luo, Z.-D. Meng, B.-W. Mao, J.-F. Li, B. Ren, J. Aizpurua, V. A. Apkarian, P. N. Bartlett, J. Baumberg, S. E. J. Bell, A. G. Brolo, L. E. Brus, et al., *Chem. Soc. Rev.* **2025**, *54*, 1453.
[89] W. Xia, Y. Xie, S. Jia, S. Han, R. Qi, T. Chen, X. Xing, T. Yao, D. Zhou, X. Dong, J. Zhai, J. Li, J. He, D. Jiang, Y. Yamauchi, M. He, H. Wu, B. Han, *J. Am. Chem. Soc.* **2023**, *145*, 17253.
[90] C. M. Gunathunge, V. J. Ovalle, Y. Li, M. J. Janik, M. M. Waegele, *ACS Catal.* **2018**, *8*, 7507.
[91] J. Wei, S.-N. Qin, J. Yang, H.-L. Ya, W.-H. Huang, H. Zhang, B. J. Hwang, Z.-Q. Tian, J.-F. Li, *Angew. Chem., Int. Ed.* **2021**, *17*, 9306.
[92] B. Wang, M. Wang, Z. Fan, C. Ma, S. Xi, L.-Y. Chang, M. Zhang, N. Ling, Z. Mi, S. Chen, W. R. Leow, J. Zhang, D. Wang, Y. Lum, *Nat. Commun.* **2024**, *15*, 1719.
[93] F. Lin, Y. Liu, X. Yu, L. Cheng, A. Singer, O. G. Shpyrko, H. L. Xin, N. Tamura, C. Tian, T.-C. Weng, X.-Q. Yang, Y. S. Meng, D. Nordlund, W. Yang, M. M. Doeff, *Chem. Rev.* **2017**, *117*, 13123.
[94] X. Y. Zhang, Z. X. Lou, J. Chen, Y. Liu, X. Wu, J. Y. Zhao, H. Y. Yuan, M. Zhu, S. Dai, H. F. Wang, C. Sun, P. F. Liu, H. G. Yang, *Nat. Commun.* **2023**, *14*, 7681.
[95] J. Timoshenko, A. Bergmann, C. Rettenmaier, A. Herzog, R. M. Arán-Ais, H. S. Jeon, F. T. Haase, U. Hejral, P. Grosse, S. Kühl, E. M. Davis, J. Tian, O. Magnussen, B. Roldan Cuenya, *Nat. Catal.* **2022**, *5*, 259.
[96] X. Ren, J. Zhao, X. Li, J. Shao, B. Pan, A. Salamé, E. Boutin, T. Groizard, S. Wang, J. Ding, X. Zhang, W.-Y. Huang, W.-J. Zeng, C. Liu, Y. Li, S.-F. Hung, Y. Huang, M. Robert, B. Liu, *Nat. Commun.* **2023**, *14*, 3401.
[97] J. Timoshenko, B. Roldan Cuenya, *Chem. Rev.* **2020**, *121*, 882.
[98] J. Song, Z. Qian, J. Yang, X. Lin, Q. Xu, J. Li, *ACS Energy Lett.* **2024**, *9*, 4414.
[99] W. Chen, X. Jin, L. Zhang, L. Wang, J. Shi, *Adv. Sci.* **2024**, *11*, 2304424.
[100] S. C. Sarma, J. Barrio, A. Bagger, A. Pedersen, M. Gong, H. Luo, M. Wang, S. Favero, C.-X. Zhao, Q. Zhang, A. Kucernak, M.-M. Titirici, I. E. L. Stephens, *Adv. Funct. Mater.* **2023**, *33*, 2302468.
[101] M. Zeng, W. Fang, Y. Cen, X. Zhang, Y. Hu, B. Y. Xia, *Angew. Chem., Int. Ed.* **2024**, *136*, 202404574.
[102] S. A. Chala, K. Lakshmanan, W.-H. Huang, A. W. Kahsay, C.-Y. Chang, F. T. Angerasa, Y.-F. Liao, J.-F. Lee, H. Dai, M.-C. Tsai, W.-N. Su, B. J. Hwang, *Appl. Catal. B: Environ.* **2024**, *358*, 124420.
[103] C.-S. Hsu, J. Wang, Y.-C. Chu, J.-H. Chen, C.-Y. Chien, K.-H. Lin, L. D. Tsai, H.-C. Chen, Y.-F. Liao, N. Hiraoka, Y.-C. Cheng, H. M. Chen, *Nat. Commun.* **2023**, *14*, 5245.
[104] L. Fang, M. Wan, Y. Liu, B. Reinhart, Z. Jin, M. Yang, F. Che, T. Li, *ACS Mater. Lett.* **2024**, *6*, 3343.
[105] W. Niu, Z. Chen, W. Guo, W. Mao, Y. Liu, Y. Guo, J. Chen, R. Huang, L. Kang, Y. Ma, Q. Yan, J. Ye, C. Cui, L. Zhang, P. Wang, X. Xu, B. Zhang, *Nat. Commun.* **2023**, *14*, 4882.
[106] Y. Liu, Z. Lou, X. Wu, B. Mei, J. Chen, J. Zhao, J. Li, H. Yuan, M. Zhu, S. Dai, C. Sun, P. Liu, Z. Jiang, H. Yang, *Adv. Mater.* **2022**, *34*, 2202568.

 

[107] J. R. Dwyer, M. Harb, *Appl. Spectrosc.* **2017**, *71*, 2051.
[108] J. Vavra, T. H. Shen, D. Stoian, V. Tileli, R. Buonsanti, *Angew. Chem., Int. Ed.* **2020**, *60*, 1347.
[109] E. Zhang, T. Wang, K. Yu, J. Liu, W. Chen, A. Li, H. Rong, R. Lin, S. Ji, X. Zheng, Y. Wang, L. Zheng, C. Chen, D. Wang, J. Zhang, Y. Li, *J. Am. Chem. Soc.* **2019**, *141*, 16569.
[110] L. DeRita, J. Resasco, S. Dai, *Nat. Mater.* **2019**, *18*, 746.
[111] N. Zhang, X. Zhang, L. Tao, P. Jiang, C. Ye, R. Lin, Z. Huang, A. Li, D. Pang, H. Yan, Y. Wang, P. Xu, S. An, Q. Zhang, L. Liu, S. Du, X. Han, D. Wang, Y. Li, *Angew. Chem., Int. Ed.* **2021**, *60*, 6170.

**Rongbo Sun** received her Ph.D. degree in Chemistry from the University of Science and Technology of China (USTC) in 2022. Subsequently, she joined Sinochem Holdings Corporation Ltd. and has been dedicated to research and development work. Her current research focuses on the development of low-carbon/negative-carbon technologies and microstructure regulation of nanomaterials. She has authored or co-authored over 21 SCI papers with an H-index of 13.

**Yuchao Wang** received his Bachelor's degree from the East China University of Science and Technology (2018). Subsequently, he received his Master's degree from Central South University of Forestry and Technology (2021). He is currently pursuing his Ph.D. degree.

**Jingjie Ge** is an Assistant Professor in the Department of Applied Biology and Chemical Technology at The Hong Kong Polytechnic University. She received her Ph.D. from the University of Science and Technology of China (USTC). Her current research focuses on the atomic precision design of nanocatalysts for green chemistry and sustainable energy. She has authored or co-authored over 40 SCI papers with an H-index of 23. She is the Young Editorial Committee Member of Nano Research, MedMat, and Materials Reports: Energy.

 